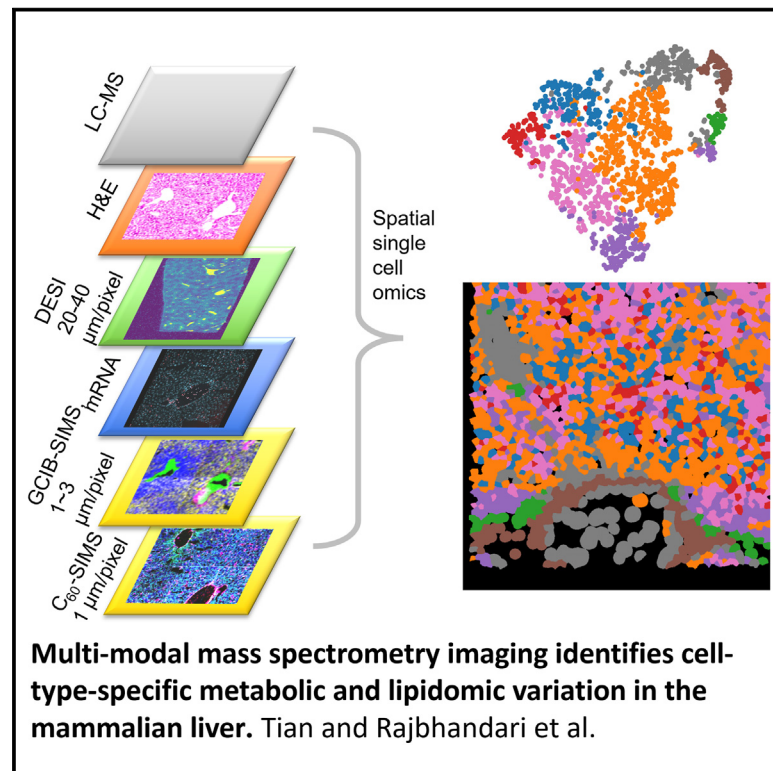


# Developmental Cell

## Multimodal mass spectrometry imaging identifies cell-type-specific metabolic and lipidomic variation in the mammalian liver

### Graphical abstract



### Authors

Hua Tian, Presha Rajbhandari,  
Jay Tarolli, ..., Gilles Frache,  
Nicholas Winograd, Brent R. Stockwell

### Correspondence

hut17@pitt.edu (H.T.),  
bstockwell@columbia.edu (B.R.S.)

### In brief

Tian and Rajbhandari et al. integrated metabolites, lipids, and proteins profiling, using a multimodal MSI workflow, and identified the lipidomic/metabolic signatures in liver functional units and different cell types.

### Highlights

- Multimodal MSI integrates the spatial multi-omics at tissue and single-cell levels
- Dual-SIMS images metabolic states of different cell types in the frozen liver
- DESI reveals zonation across liver tissue functional units

Article

# Multimodal mass spectrometry imaging identifies cell-type-specific metabolic and lipidomic variation in the mammalian liver

Hua Tian,<sup>1,2,10,\*</sup> Presha Rajbhandari,<sup>3,10</sup> Jay Tarolli,<sup>4</sup> Aubrianna M. Decker,<sup>3</sup> Taruna V. Neelakantan,<sup>5</sup> Tina Angerer,<sup>6,7</sup> Fereshteh Zandkarimi,<sup>5</sup> Helen Remotti,<sup>8</sup> Gilles Frache,<sup>6</sup> Nicholas Winograd,<sup>9</sup> and Brent R. Stockwell<sup>3,5,8,11,\*</sup>

<sup>1</sup>Environmental and Occupational Health, Pitt Public Health, Pittsburgh, PA 15261, USA

<sup>2</sup>Children's Neuroscience Institute, School of Medicine, Pittsburgh, PA 15224, USA

<sup>3</sup>Department of Biological Sciences, Columbia University, New York, NY 10027, USA

<sup>4</sup>Ionpath Inc., Menlo Park, CA 94025, USA

<sup>5</sup>Department of Chemistry, Columbia University, New York, NY 10027, USA

<sup>6</sup>The Luxembourg Institute of Science and Technology, 4362 Esch-sur-Alzette, Luxembourg

<sup>7</sup>Department of Pharmaceutical Biosciences, Uppsala University, 751 05 Uppsala, Sweden

<sup>8</sup>Department of Pathology and Cell Biology, Vagelos College of Physicians and Surgeons, Columbia University Irving Medical Center, New York, NY 10032, USA

<sup>9</sup>Department of Chemistry, Pennsylvania State University, University Park, PA 16802, USA

<sup>10</sup>These authors contributed equally

<sup>11</sup>Lead contact

\*Correspondence: [hut17@pitt.edu](mailto:hut17@pitt.edu) (H.T.), [bstockwell@columbia.edu](mailto:bstockwell@columbia.edu) (B.R.S.)

<https://doi.org/10.1016/j.devcel.2024.01.025>

## SUMMARY

Spatial single-cell omics provides a readout of biochemical processes. It is challenging to capture the transient lipidome/metabolome from cells in a native tissue environment. We employed water gas cluster ion beam secondary ion mass spectrometry imaging ( $[\text{H}_2\text{O}]_{n>28\text{K}}\text{-GCIB-SIMS}$ ) at  $\leq 3 \mu\text{m}$  resolution using a cryogenic imaging workflow. This allowed multiple biomolecular imaging modes on the near-native-state liver at single-cell resolution. Our workflow utilizes desorption electrospray ionization (DESI) to build a reference map of metabolic heterogeneity and zonation across liver functional units at tissue level. Cryogenic dual-SIMS integrated metabolomics, lipidomics, and proteomics in the same liver lobules at single-cell level, characterizing the cellular landscape and metabolic states in different cell types. Lipids and metabolites classified liver metabolic zones, cell types and subtypes, highlighting the power of spatial multi-omics at high spatial resolution for understanding cellular and biomolecular organizations in the mammalian liver.

## INTRODUCTION

Technological advances in the past decade have enhanced spatial single-cell multi-omics to address multi-level heterogeneities in tissues. Great efforts are underway to map the diversity of cell types and subtypes with biomarkers in healthy and disease tissues, such as the Human Biomolecular Atlas Program (HuBMAP),<sup>1</sup> the Human Tumor Atlas Network (HTAN),<sup>2</sup> and the Kidney Precision Medicine Project (KPMP<sup>3</sup>).<sup>4</sup> There is an explosion of single-cell transcriptomics and proteomics for such efforts. However, spatial metabolomics, a readout of phenotypes and molecular networks at the genomic, transcriptomic, and proteomic levels, remains less explored.<sup>5–7</sup> Mass spectrometry imaging (MSI) is the primary method for spatial metabolomics, enabling multiplexed mapping of untargeted molecular species within cells and tissue. Commonly used MSI technologies include desorption electrospray ionization (DESI)<sup>8</sup> and matrix-assisted laser desorption ionization (MALDI).<sup>9</sup> DESI is an ambient

ionization technique with preferential ionization and characterization of metabolites and lipids at a spatial resolution as high as  $30 \mu\text{m}$ .<sup>7</sup> MALDI is utilized for lipids, abundant proteins, and metabolites with a suitable matrix at an achievable spatial resolution of  $5\text{--}10 \mu\text{m}$ .<sup>10</sup>

However, practical application of MSI at single-cell resolution has been challenging. First, detection limits hinder imaging of low concentrations of biomolecules, as detectable signals decrease significantly in smaller pixels. Second and critically, cryogenic analysis, an approach to maintain pristine chemical gradients, is not widely applicable to most MSI tools. Fresh-frozen tissue retains cellular content at a near-native state, especially for dynamic and transient metabolites. Finally, due to the incompatibility of sample preparation and the difficulty of preserving dynamic metabolic gradients,<sup>11</sup> it is nearly impossible to acquire multi-omic data on the same sample or to spatially co-localize molecules at the single-cell level.

To overcome these hurdles, a buncher-time-of-flight (ToF) SIMS, coupled with a high-voltage water gas cluster ion beam  $(\text{H}_2\text{O})_n$  ( $n > 28\text{K}$ )-GCIB and a dual-SIMS workflow,<sup>12</sup> has been developed and coupled with DESI and liquid chromatography-tandem mass spectrometry (LC-MS/MS) analyses. The first step takes advantage of intact biomolecular imaging (up to  $m/z$  5,000) at an achievable spatial resolution of up to  $\sim 1 \mu\text{m}$ , using a newly designed GCIB operating at  $\sim 70 \text{ kV}$ .<sup>11,13</sup> Coupled with cryogenic sample handling, frozen-hydrated biosamples are transferred under nitrogen atmosphere and imaged in a near-native state (at 100 K). Subsequently, cell-type-specific and structural proteins are mapped in the same sample stained with a panel of lanthanide-conjugated antibodies, using  $\text{C}_{60}$ -SIMS at  $1 \mu\text{m}$  resolution. This development allowed simultaneous mapping of metabolites, lipids, and peptides in the same tissue section, with single-cell resolution and high sensitivity.<sup>11,12</sup> Building on single-cell imaging by dual-SIMS, we incorporated other imaging modalities (e.g., DESI, MALDI, hematoxylin and eosin [H&E], and mRNA scope) as well as LC-MS/MS and AI-aided computational processing (DeepCell) to achieve multi-omic imaging of liver tissue architecture at both tissue level and single-cell level.

We applied this pipeline to liver tissue, a critical metabolic hub that performs uptake and storage of nutrients, metabolism, bile secretion, detoxification, protein synthesis, and immune functions.<sup>14</sup> The hepatic parenchyma exhibits metabolic zonation to facilitate these functions, based on the gradient of oxygen-and-nutrient-rich blood along the portal triad (PT) to central vein (CV) axis. The periportal (PP) region surrounding the PT receives a maximum amount of nutrients and oxygen, being responsible for oxidative metabolism, including  $\beta$ -oxidation, gluconeogenesis, bile formation, and cholesterol synthesis. The pericentral (PC) region surrounding the CV receives less oxygen and nutrients, mainly conducting detoxification, ketogenesis, lipogenesis, glycolysis, glycogen synthesis, and glutamine synthesis.<sup>15,16</sup>

Within the liver parenchyma, hepatocytes make up 70% of the cell population and are metabolically heterogeneous along the porto-central axis. Although hepatocytes in different zones appear homogeneous morphologically, they are metabolically distinct, displaying zonal preferences of metabolic enzymes involved in oxidative energy, carbohydrate, lipid, and nitrogen metabolism. These enzymes include carbamoylphosphate synthetase (CPS1), glutamine synthetase (GS), and cytochrome P450, family 2, subfamily AE, polypeptide1 (Cyp2ae1).<sup>17</sup> The heterogeneity of the liver extends to the cellular level, with highly organized multiple cellular structures executing essential liver functions. Non-parenchymal cells, including macrophages (Kupffer cells), liver sinusoidal endothelial cells, and hepatic stellate cells, are located within the hepatic sinusoids and play a critical role in interacting with and regulating parenchymal cells.<sup>18</sup> Liver zonation and function have mainly been explored with immunohistochemistry (IHC) and single-cell spatial transcriptomics<sup>16,19</sup>; however, mapping lipids and metabolites in single cells has lagged. Metabolites and lipids are often altered in liver diseases and are vital effector molecules in metabolic pathways.<sup>20,21</sup>

Here, we present a multimodal MSI approach centered on DESI,  $(\text{H}_2\text{O})_n$ -GCIB-SIMS, and  $\text{C}_{60}$ -SIMS (dual-SIMS) for mapping of unlabeled endogenous metabolites and lipids, and targeted proteins within anatomical structures and cell types, providing a

powerful approach to explore integrated spatial biology in mouse and human liver. This workflow is complemented by histological (H&E) staining for anatomical structure annotation and multimodal image alignment, RNAscope for mRNA transcript profiling of landmark genes<sup>22</sup> for zonal antibody validation, and MALDI Orbitrap MSI for ion species confirmation. Moreover, ultra-high performance liquid chromatography (UPLC) coupled with electrospray ionization (ESI) tandem mass spectrometry (MS/MS) is adapted for lipid confirmation in DESI and SIMS experiments. Heterogeneities in liver tissue were detected by a combination of metabolites, lipids, and proteins in human and mouse liver, including sex-specific zonation patterns, functional-specific zonation, and potential metabolic states of different cell types. We found that lipid and metabolite composition may classify liver zonation and cell types. The multimodal workflow we present for single-cell multi-omic imaging allows for an unprecedented understanding of multi-level heterogeneities, metabolic cell states, coordinated molecule networks, and cell identity.

## RESULTS

### Multimodal imaging centered on mass spectrometry imaging technologies generates a spatial multi-omic atlas of liver tissue

To comprehensively assess the spatial organization of liver tissue with regard to its cellular, metabolic, and lipidomic heterogeneities, we performed multimodal imaging on consecutive tissue sections of mouse and human liver, using DESI, H&E, dual-SIMS, and RNAscope (Figure 1). DESI was employed to image an entire tissue section at a spatial resolution of  $40 \mu\text{m}$  in both positive and negative ion modes. More than 100 lipid and metabolite features were extracted, and ion species localized to the PP and PC regions (Figure 1A) were identified. Guided by DESI and H&E images, a region containing both PT and CV was selected on consecutive tissue sections for dual-SIMS imaging on a serial fresh-frozen tissue with single-cell resolution (Figure 1B). We implemented a technological development using a three-step process: first, cryogenic  $(\text{H}_2\text{O})_n$ -GCIB-SIMS was performed to localize  $>200$  lipid and metabolites in a pristine native environment at  $3 \mu\text{m}$  per pixel, followed by immunostaining with a panel of lanthanide-conjugated antibodies specific to liver biology (key resources table) on the same tissue section.  $\text{C}_{60}$ -SIMS was then utilized to image metal-labeled antibodies to map the cell landscape and tissue structure at  $1 \mu\text{m}$  per pixel. As  $(\text{H}_2\text{O})_n$ -GCIB-SIMS removes about 100 nm of material from the tissue surface, the antibody markers stain the same cells as those from which lipids and metabolites are detected. This approach facilitated image alignment and cell segmentation to register multi-omics data to the same cells on a single section, elucidating biomolecular complexity within different cell types directly in native tissue content without dissociation, which is otherwise difficult to integrate.

For validation of several zonation and cell-type-specific markers, RNAscope was performed on a consecutive tissue section for transcriptomic analysis (Figure 1D). To confirm ion species assignment by accurate mass and fragmentation pattern, we performed (1) MALDI on an Orbitrap, performed on the serial sections for *in situ* MS/MS analysis (Figure 1C), and (2) lipidomics analysis using UPLC with ion mobility ToF MS<sup>E</sup> (HDMS<sup>E</sup>) data-independent acquisition and analysis (Figure 1F).

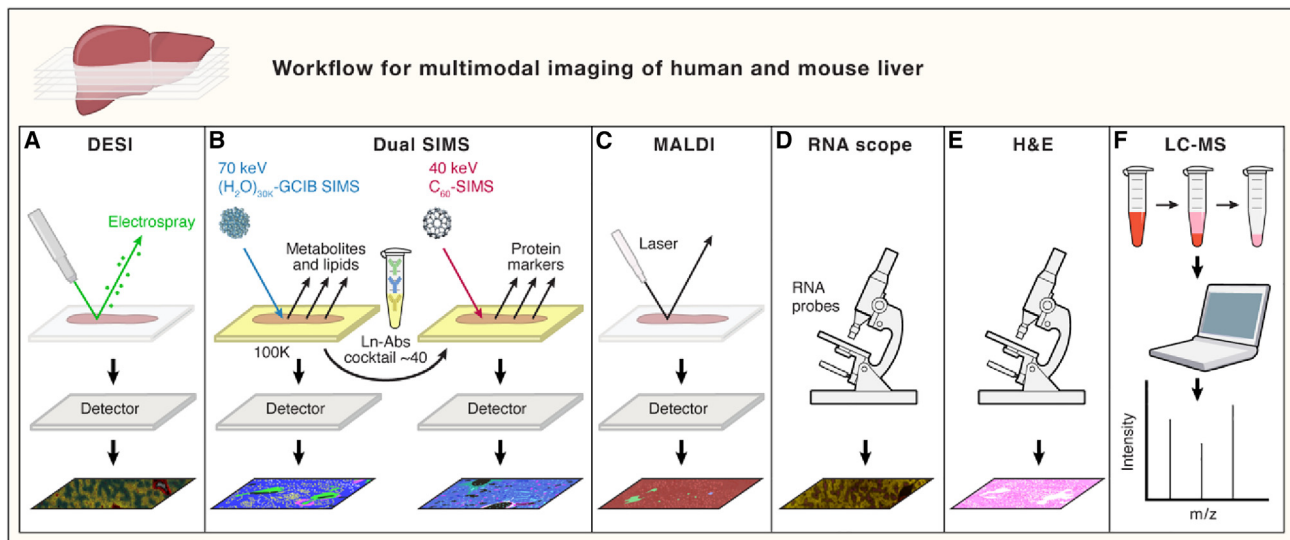


**Figure 1. Schematics of MSI-centric multimodal imaging workflow reveals 2D/3D biomolecular atlas of liver**

(A and B) Consecutive sections from liver tissue blocks are assessed by (A) DESI-MSI exhibiting the distribution of lipids and metabolites within histologically defined structural units of liver within the tissue architecture and by (B) SIMS-MSI including  $(\text{H}_2\text{O})_n^+$ -GCIB-SIMS for lipid and metabolite imaging at single-cell resolution, followed by  $\text{C}_{60}^+$ -SIMS on the same tissue section, followed by image integration and single-cell-specific lipid and metabolite extraction. (C and D) (C) MALDI validation of lipids detected by DESI and SIMS, and (D) RNAscope validation of major antibody markers. (E) H&E image of serial liver section for annotation of morphological features and guidance of MSI imaging. (F) Parallel LC-MS/MS analysis for second validation of species annotation.

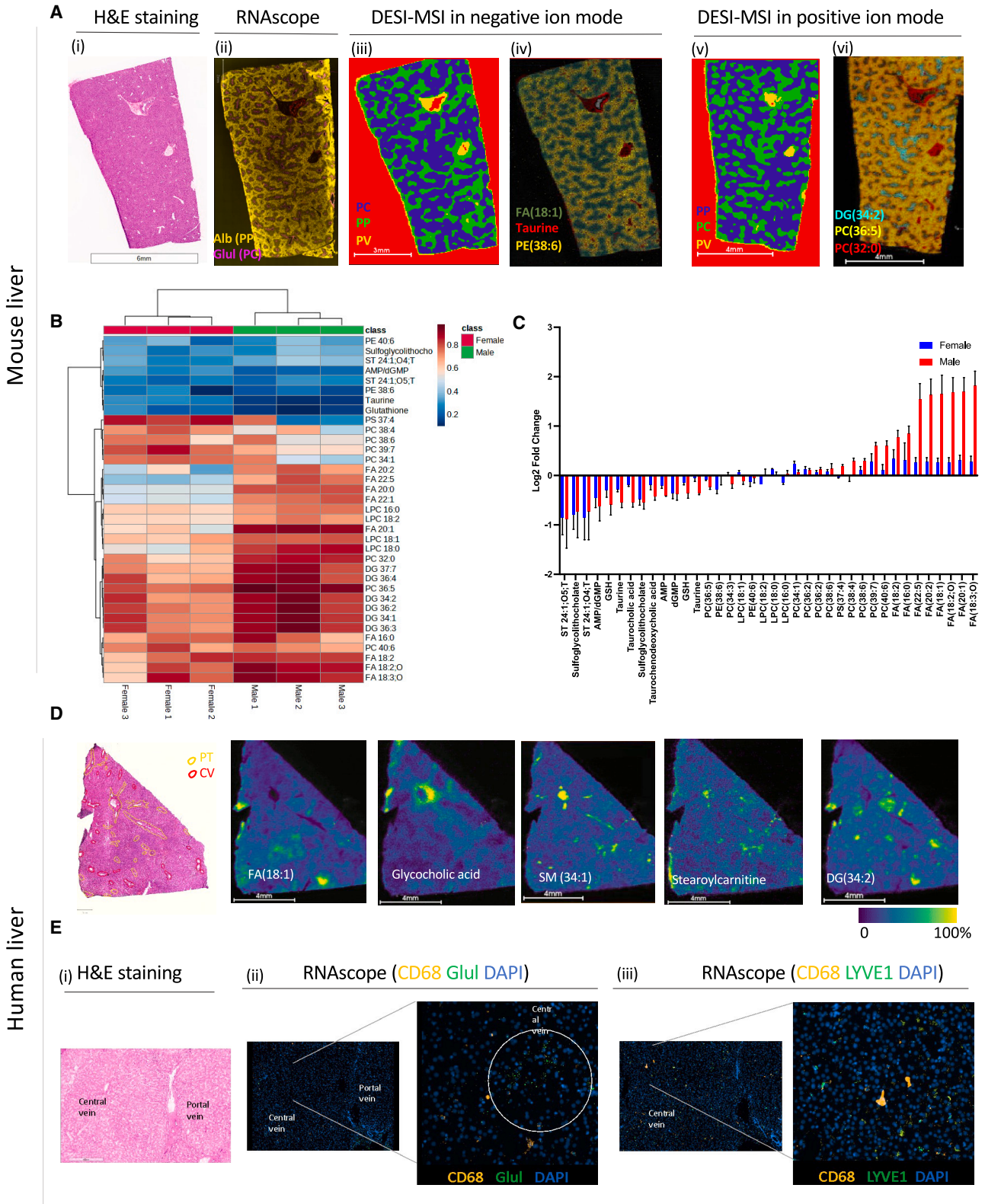
This was followed by computational data processing for cellular and structure segmentation, omics integration, and discriminant analysis. Our current work improved a previous workflow<sup>12</sup> using cross-validation of three MSI modalities and LC-MS/MS, AI-aided computational processing for precise cell segmentation, and comprehensive visualization at tissue and single-cell levels. 2D/3D image reconstruction was performed to visualize molecular and cellular heterogeneities, showing distinct molecular clusters in metabolic zones, omics spatial networks, and the cellular landscape in the PT region in human liver.

### DESI-MSI reveals metabolic zonation-specific metabolites and lipids in mouse liver

To evaluate metabolite and lipid distribution with metabolic zones, liver tissues from 6 different mice (3 male and 3 female) were examined histologically. H&E-stained images were annotated to identify the PT and CV regions, showing uniform distribution patterns within the tissue (Figures 2Ai and S1A). The annotation was then validated by transcript and protein markers targeting metabolic enzymes that are specific to PP and PC regions.<sup>17</sup> For example, albumin (*Alb*) was concentrated in the PP region, and glutamine synthetase (*Glu1*) was localized in the PC region, using RNAscope, respectively (Figures 2Aii and S1B). The distributions were consistent with previous work<sup>19</sup>; however, we noted sex-linked differences. *Alb* was concentrated more around the PP zone in male mice, whereas it expanded toward the CV in female mice. *Glu1* expression has been previously shown to exhibit sex-specific variation in different mouse and rat strains.<sup>23</sup> However, we observed a similar distribution pattern in the male and female C57BL/6 mice strains used in this study.

DESI imaging of mouse liver identified essential metabolites and lipids in both positive and negative ion modes. In positive ion mode, lipid classes such as glycerophospholipids and glycerolipids were observed (Tables S1A and S1B). In negative ion mode, more diverse species were observed, including free fatty acids (FAs) and small metabolites in a low  $m/z$  range ( $m/z$  100–400), glycerophospholipids in the high  $m/z$  range ( $m/z$  700–800), and conjugated bile acids (Tables S1A and S1B). To extract PP-specific and PC-specific lipids and metabolites, we first sought to create a segmentation mask for these regions within tissue sections. A few ion species ( $m/z$  124.01, 280.23, 282.25, 306.07, and 309.28 in negative ionization mode and  $m/z$  534.29, 631.47, 734.57, 794.51, 802.5, and 852.55 in positive ionization mode) exhibiting unique distribution patterns (Figures 2Aiv, 2Avi, and S1) were used to perform bisecting k-means clustering with Euclidean distance, within the SCiLS software platform. Spatial segmentation was performed with edge-preserving denoising to remove pixel-to-pixel variability observed in MSI datasets.<sup>24</sup> This resulted in PP and PC clusters in individual mouse liver tissue sections in both positive and negative ion modes, shown as a segmentation map (Figures 2Aii, 2Av, S1C, and S1D).

The cluster specificity was confirmed by comparing *Alb* and *Glu1* transcript distribution with DESI segmentation (Figures S1B, S1C, and S1D). To identify lipids and metabolites that discriminate PC versus PP clusters, we implemented a binary classifier—receiver operating characteristic (ROC)-area under the curve (AUC) analysis.<sup>25,26</sup> Each tissue-specific ion was evaluated for its discriminating power, using a threshold of the (AUC >0.70 to be considered a classifier. We observed that metabolites such as glutathione (GSH), taurine, and conjugated bile acids were zoned in PP region (Figures 2B, S1G, and S1H). Our results were complementary to previous results on the metabolic gradients



(legend on next page)

from PC to PP: liver bile acids are primarily synthesized in PC hepatocytes; they flow toward the bile duct, and the enzymes cascade involved in bile acid biosynthesis is organized spatially. In particular, the enzyme conjugating bile acids is abundant in PP region, where taurine also comes in from blood supply.<sup>19,27</sup>

As noted, we observed sexual dimorphism in the distribution of several lipid species. While previous studies have shown sex-specific differences in lipid metabolism, it has not been shown in the spatial context within liver.<sup>28,29</sup> Diacylglycerols (DGs) and free FAs were zoned in the PC region (Figures 2B, S1E, and S1F), with the average ROC-AUC for individual DG ions >0.89 for males and >0.7 for females (Figure 2B). Compared with females, male mice showed higher amounts of DGs in PC versus PP zones (log<sub>2</sub> fold change of ~1.5 for males and 0.4 for females) (Figure 2C). Similar observations were made for FAs (Figures 2B, 2C, and S1F). While some FAs such as FA (18:1), FA (20:1), FA (18:3;O), FA (18:2), and FA (20:0) showed high specificity for PC versus PP zone, with the average ROC-AUC for individual ions >0.88 for males and >0.7 for females (Figure 2B), others such as FA (18:2;O), FA (16:0), FA (22:5), and FA (20:2) exhibited higher specificity for PC zones in males versus females, with the average ROC-AUC for individual ions >0.73 for males and <0.57 for females. FA (20:0) and FA (18:3;O) showed relatively higher abundance in PC versus PP in both male and female mice, and FA (20:1) and FA (22:5) showed minimal differences between the regions in female mice (Figures 2C and S1F).

The PC region has previously been reported to exhibit a higher degree of lipogenesis, FA synthesis, and acetyl CoA carboxylase expression than the PP zone.<sup>30,31</sup> Phospholipids, including phosphatidylcholine (PC) and lysophosphatidylcholine (LPC), did not exhibit a specific pattern. Some lipids (e.g., PC (40:6)) showed similar distribution between the PP and PC zones, while others (e.g., PC (36:5), PC (32:0), and PC (34:1)) exhibited differential distributions between regions or between regions and sexes (e.g., LPC (18:2), LPC (18:0), LPC (16:0), PC (38:4), and PC (39:7)) (Figures 2B, 2C, and S1I). Thus, while male and female mice have histologically and morphologically similar livers, they are metabolically distinct.

### DESI-MSI reveals zonation-specific metabolites and lipids in human liver

The DESI workflow was then performed on consecutive tissue sections from human liver. H&E staining was again performed to assess tissue morphology and annotate PP and PC regions (Figure 2D). RNAscope was used to validate *Glul* staining, which un-

like in mouse liver, appeared as dispersed puncta around the CV region (Figure 2Eii). This is likely due to lower expression of the gene in human liver and needs further optimization. Hence, PP and PC regions were annotated manually based on H&E staining (Figure 2D).

DESI imaging at 40 μm spatial resolution showed similar average mass spectra profiles in both positive and negative ion modes, compared with mouse liver. The annotated species are in Tables S1A and S1B. Taurine-conjugated and glycine-conjugated bile acids were abundant in the PT and PP region, as well as in the septa connecting the neighboring PTs, showing similar functional zonation between human and mouse liver (Figure 2D). The vasculature was identified by the abundance of the marker heme B. Cholesterol, a precursor to bile acids, was concentrated within the portal vein (PV) and CV regions. Sphingomyelins (SMs), including SM 34:1, were co-localized with cholesterol (Figure 2D), where SMs are postulated to form hydrophobic lipid raft domains with cholesterol, preventing hepatic damage from bile salts and also playing a role in pathophysiology.<sup>32,33</sup> Similarly, stearyl carnitine was localized in the PP region (Figure 2D), where acyl carnitines play an important role in transferring long-chain FAs to mitochondria for β-oxidation.<sup>34</sup> Several small metabolites and lipid species exhibited differential distributions in human tissue (Figure 2D). FAs, DAGs, and triglycerides (TAGs) exhibited distinct distribution patterns that, unlike in mouse tissue, did not overlay with the PC region (Figure 2D). This could stem from the complexity of human liver, where metabolic gradients are more dynamic and heterogeneous, based on a person's genetic profile and changes in gene expression and metabolic-enzyme-based factors, such as diet, hormones, gender, and underlying pathology.<sup>15,35</sup> Similarly, varied patterns of phospholipid species were observed within the liver.

In addition to 2D imaging of tissue sections, we postulated that 3D DESI would aid visualization of the distribution of lipids and metabolites within 3D tissue structures and gradients with respect to tissue depth, capturing branching of blood flow and anatomic structure. We generated a 3D model visualizing differentially distributed lipids by performing DESI on serial sections (Video S1) and observed consistent distribution of lipids and metabolites along the tissue depth.

### SIMS imaging delineates heterogeneities of multiple biomolecules and cell types at single-cell level in mouse liver

To associate lipids and metabolites with cell types in the liver, dual-SIMS imaging at spatial resolution of 1–3 μm was

#### Figure 2. DESI-MSI reveals periportal- and pericentral-specific lipids and metabolites in mouse and human liver

- (A) (Ai) H&E staining performed on a normal mouse liver section to identify the central vein (CV) and portal triad (PT) regions. (Aii) RNAscope is performed on a consecutive tissue section stained for expression of albumin (*Alb*; yellow) and glutamine synthetase (*Glul*; magenta), showing differential staining for periportal (PP) and pericentral (PC) regions, respectively. (Aiii and Av) Spatial segmentation of pixels based on distributions of a few lipids and metabolites from DESI-MSI in (Aiii) negative and (Av) positive ion modes. (Aiv and Av) Distribution of a few lipids and metabolites showing PC and PP specificity in both ion modes are shown.
- (B) Heatmap depicting the predictive performance of features measured by AUC-ROC (in rows) and classification (in columns) from DESI for PP and PC regions in female (n = 3) and male (n = 3) mouse liver sections.
- (C) Fold change values comparing the mean intensity of PC versus PP regions for the features from (B). Error bars represent mean ± standard deviation.
- (D) H&E section with manual annotation of CV and PT regions in human liver section. The corresponding images for distribution of different classes of lipids are shown.
- (E) Fluorescent RNAscope image of cell markers in human liver. H&E staining in (Ei) and corresponding RNAscope image on the serial section showing distribution of (Eii) macrophages (CD68) in yellow, glutamine synthetase (*Glul*) in green, and nuclear staining (DAPI) in blue. (Eiii) macrophages (CD68) in yellow, sinusoidal endothelial cells (LYVE1) in green, and nuclear staining (DAPI) in blue.

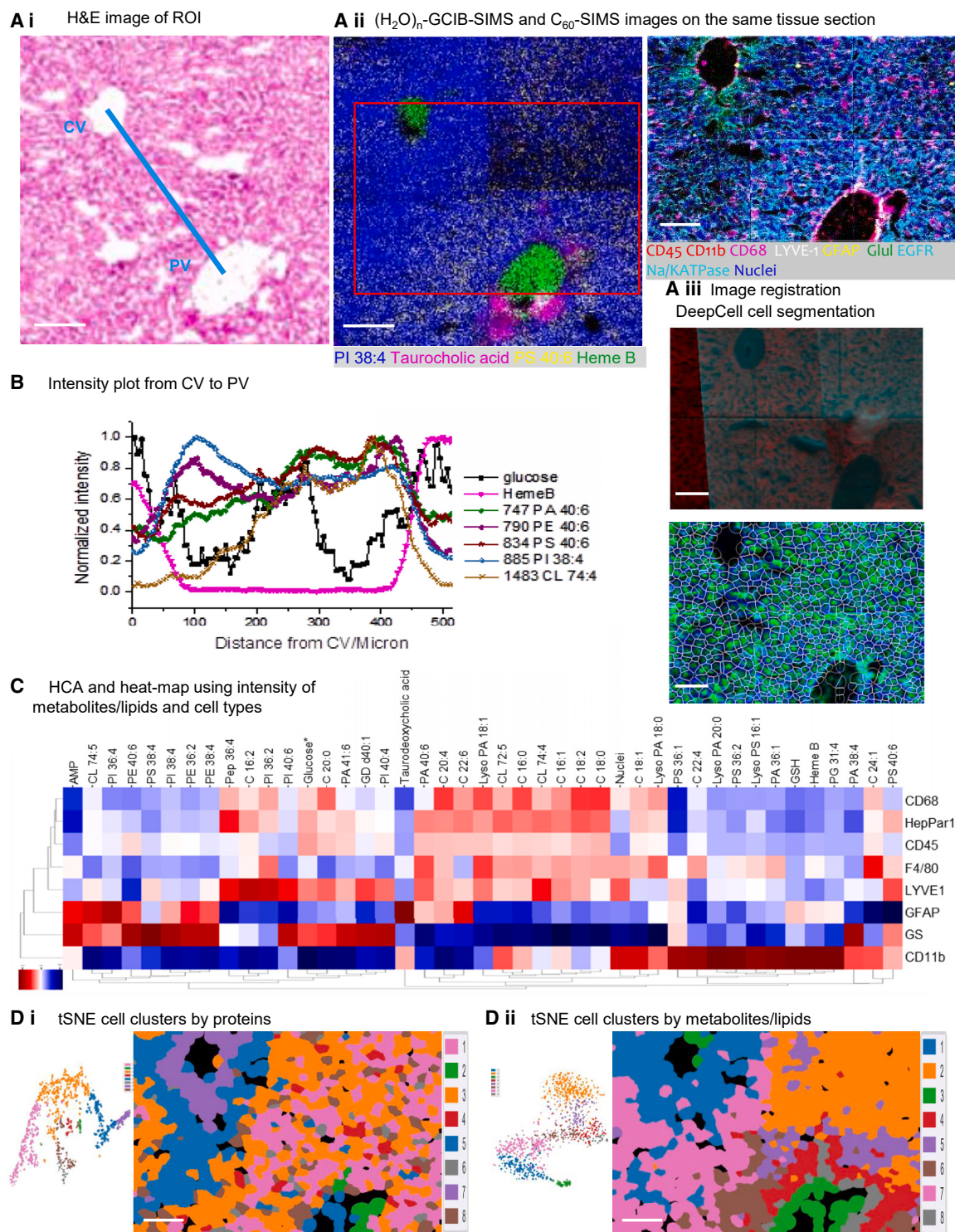


**Figure 3. Dual high-resolution SIMS imaging delineates the metabolomic and lipidomic states in different cell types on the mouse liver section**

(A) (A i) H&E staining image of central vein (CV) and portal vein (PV) region.

(A ii) Representative color overlay images of dual-SIMS. Metabolite and lipid image in the same region as in (A i) on a serial frozen-hydrated section using  $(\text{H}_2\text{O})_n$ -GCIB-SIMS at a spatial resolution of  $3 \mu\text{m}$ . Blue, PI 38:4; magenta, taurocholic acid; yellow, PS 40:6; green, heme B. More single-species images are in [Figure S2](#). Protein image by lanthanide-conjugated antibodies from the region highlighted in the red box, using  $\text{C}_{60}$ -SIMS at a spatial resolution of  $1 \mu\text{m}$ . Red, CD45 and CD11b; yellow, GFAP; white, LYVE-1; magenta, F4/80 and CD68; cyan, EGFR and Na/KATPase; green, Glul; blue, nuclei.

(legend continued on next page)

performed on consecutive mouse liver sections. Guided by H&E-stained images, a region of interest (ROI) containing both CV and PV was selected (Figure 3Ai) for  $(\text{H}_2\text{O})_n$  ( $n=30k$ )-GCIB-SIMS imaging in negative ion mode, mapping more than 100 lipids and metabolites. These species were heterogeneous around CV and PV, including nucleotides, bile acids, glucose (with isomeric forms), FAs, phosphatidylinositols (PIs), phosphatidylserines (PSs), lysophosphatidylserines (LPSs), phosphatidic acids (PAs), and lysophosphatidic acids (LPAs). PI (38:4) was highly concentrated in the PC region, and PS (40:6) distributed in complementary locations with an elevated concentration around the PP region. Heme B was mainly present inside veins, while taurocholic acid was present in the PP region (Figures 3Aii and S2A). In the same region, 10 cell-type-specific and tissue structure markers illuminated a heterogeneous cell landscape and recapitulated anatomical structures in the mouse liver (Figure 3Aii). The single ion images and list of selected species are detailed in Figure S2 and Table S1C, exhibiting various distribution patterns.

Except for the representative species in Figure 3Aii, principal-component analysis (PCA) revealed clusters of ions that contribute to the major features around the CV and PV. Heme B, a marker for the vasculature, was highly concentrated inside the vein in principal component 2 (PC2). As an essential lipid constituent of mitochondrial membranes, cardiolipins (CLs) were elevated around the PV rather than the CV, in line with the oxygen gradient captured in PC4.<sup>36</sup> PC5 highlighted the CV region, with elevated species such as PI (38:4), PS (38:4), PA (38:4), LPA (18:0), FA (20:4), and PS (38:3). On the other hand, PC6 showed the radiated gradient around the PV with dominant species LPS (16:1) and LPS (16:0). The chemical gradients of these species were measured along the porto-central axis by line scanning (Figure 3B). Glucose isomeric forms appeared more abundant inside the CV and PV, the same as heme B. GSH and AMP had similar patterns as glucose species, indicating high abundance of energy-related metabolites in the CV and PV region. Most PI species were concentrated around the CV region (e.g., PI (38:4)), while PA and PS species were higher in the PV region (e.g., PA (40:6), PS (40:6)). PE (40:6) appeared to be more intense at the edge of the CV and PV, contributing to the curved structure and mechanical resistance facilitated by the conical shape of PE.

Sequential  $\text{C}_{60}$ -SIMS imaging on the same region profiled by  $(\text{H}_2\text{O})_n$  ( $n=30k$ )-GCIB-SIMS further revealed the distribution of targeted protein markers, using a panel of lanthanide-labeled antibodies. The panel was designed to identify major cell types, immune cells, cell boundaries, and zonation markers within liver (key resources table). Leukocytes, myeloid cells, Ito stellate cells, sinusoidal endothelial cells, and macrophages/Kupffer cells were localized with the markers cluster of differentiation 45 (CD45) in red, cluster of differentiation molecule 11b (CD11b) in red, glial fibrillary acidic protein (GFAP) in yellow, lymphatic vessel endothelial hyaluronan receptor 1 (LYVE-1) in white, and cluster of differentiation 68 (CD68) and F4/80 in

magenta, respectively (Figures 3Aii and S3A). As expected, Glul (in green) expression was abundant around CV, which is consistent with RNAscope results. Epidermal growth factor receptor (EGFR) and sodium potassium ATPase (Na/K-ATPase) (in cyan) outlined cell borders, facilitating cell segmentation and image alignment to register multiple lipids and metabolites in individual cells Figure S3.

Image processing for alignment, registration, and cell segmentation by Deepcell<sup>37</sup> were shown in Figure 3Aiii. With this, the detected omics molecules using dual-SIMS imaging, were registered to individual segmented cells for further statistical analysis. A hierarchical clustering algorithm (HCA) compared the intensity variation of monitored metabolites/lipids among different cell types, providing a comprehensive view of cell signatures and metabolic state. Glul-expressing cells comprised significant PI (38:4), which metabolizes to downstream signaling molecules phosphatidylinositol phosphate (PIPs), known to bind many proteins and to control protein-protein interactions.<sup>38</sup> PE (40:6) also contributed to Glul-positive cells, particularly cells in the inner circle of the CV and also in the hepatocytes lining PV. Along with PA (38:4), lipids such as PS (38:4), GD (d40:1), PI (40:6), PE (38:4), PI (40:4), PE (36:2), FA (20:0), PA (41:6), and PI (36:4) were more abundant in Glul-positive cells around the CV. The glucose content was highest among the CD11b-positive cells, suggesting a glucose-dependent metabolism. Sinusoidal cells labeled by LYVE-1 were rich in lipids with a low degree of unsaturation. Cells expressing the PP hepatocyte-specific marker (HepPar1/CPS1) consisted of a higher level of LPAs and CLs (Figure 3C).

Next, t-distributed stochastic neighbor embedding (t-SNE) was performed to cluster the single-cell data points that integrate omics molecules detected using SIMS, demonstrating that metabolites and lipids classify the cell populations. Clusters 1–8 highlighted features around the PP and PC regions by proteins (Figure 3Di) and metabolites/lipids (Figure 3Dii), where the same-colored clusters shared similar distributions. Green clusters surrounded the CV region, and red clusters surrounded the green clusters, indicating that the Glul-positive cells have distinguishable metabolic/lipidomic combinations associated with different biological processes. Brown (Figure 3Di) and magenta (Figure 3Dii) clusters identified the portal endothelial cells and immune cells that are consistent with the localization of LYVE-1-, CD68-, and CD45-positive cells. The cell clusters by metabolites/lipids (purple, brown, blue, and orange in Figure 3Dii) were co-localized with HepPar-1-positive cells (blue in Figure 3Di). Hence, the abundance of metabolites and lipids allows not only for classification of cell types similar to the protein markers but also for clustering of cells into distinct metabolic subpopulations that are not captured by conventional protein markers.

### SIMS delineates cell-type-specific multi-omics at the single-cell level in human liver

The same workflow of dual-SIMS imaging was applied to PT on a human liver section (Figure 4). The high-resolution images

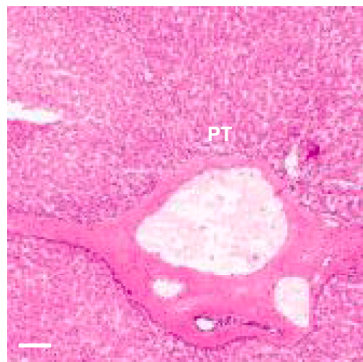
(Aiii) Registration of  $(\text{H}_2\text{O})_n$  ( $n=30k$ )-GCIB-SIMS and  $\text{C}_{60}$ -SIMS images for alignment; single-cell segmentation using DeepCell.

(B) Intensity changes of various species from center of CV to PV (as the blue line in Ai).

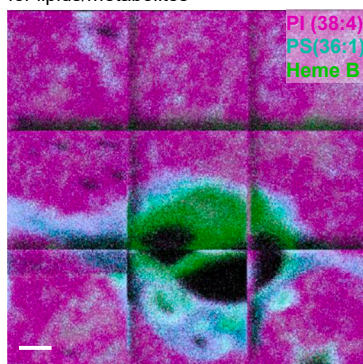
(C) HCA map shows variation of different metabolites/lipids in various types of cells.

(D) (Di) t-SNE clustering to classify cell types as in cluster 1–8 by protein markers. (Dii) t-SNE clustering to classify the cell types as in cluster 1–8 by lipids and metabolites only. Scale bars, 100  $\mu\text{m}$ .

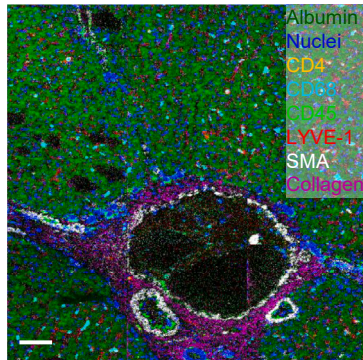
**Ai** H&E image of ROI



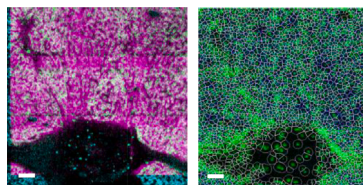
**Aii**  $(\text{H}_2\text{O})_n$ -GCIB-SIMS for lipids/metabolites



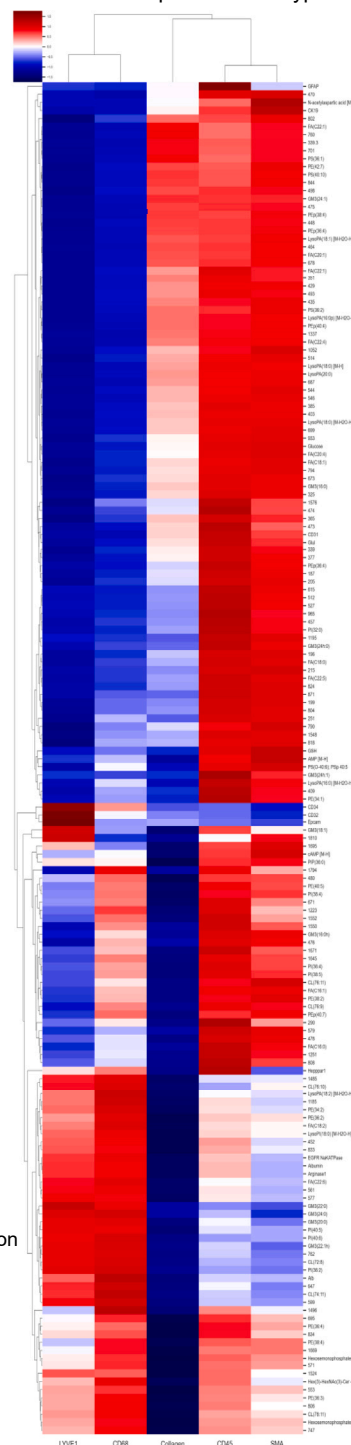
**Aiii** C60-SIMS for proteins on the same tissue



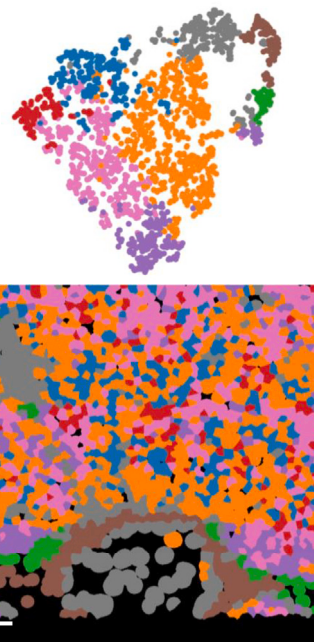
**Aiv** Image registration and cell segmentation



**B** HCA and heat-map using intensity of metabolites/lipids and cell types



**Ci** tSNE cell clusters by proteins



**Cii** tSNE cell clusters by metabolites/lipids

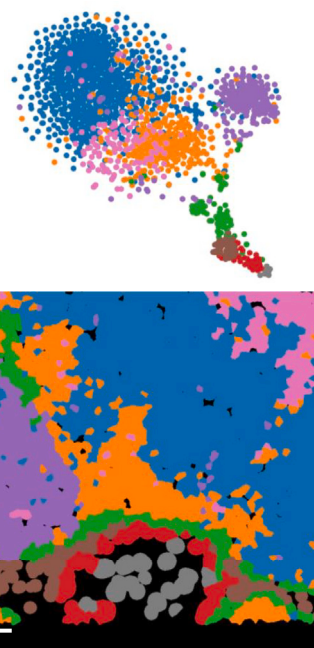


**Figure 4. Dual high-resolution SIMS imaging delineates the metabolomic and lipidomic states in different cell types on the human liver tissue section**

(A) (Ai) H&E image. The selected region contains the portal triad. Representative color overlay images of dual-SIMS in (Aii) and (Aiii). (Aii) Metabolites and lipids image in the same region as in (Ai) on a serial frozen-hydrated section using  $(\text{H}_2\text{O})_n$ -GCIB-SIMS imaging at the spatial resolution of 3  $\mu\text{m}$ . Blue, PS 36:1; magenta, PI 38:4; green, heme B. More single-species images are in [Figure S4](#).

(legend continued on next page)

revealed the heterogeneous biomolecules; as PS (36:1) outlined the PT, PI (38:4) was localized outside the PT primarily, and heme B was inside of the PT (Figure 4Aii). The single-ion images and list of 246 metabolites and lipids are in Figure S4 and Table S1C; among them, 120 species were annotated.

PCA analysis distinguished two anatomical features and metabolic flux around the PT. The PT ring has abundant PS (36:1), PA (36:1), and PI (38:4), with significant higher PS (36:1) that defines the PT region. Inside the PT ring, heme B and several PA species were dominant. The metabolic flux also showed anti-correlated patterns, with taurodeoxycholic acid/taurodeoxycholic, FA (C18:2) and FA (C18:1), taurocholic acid, and PEP (40:6) to the left of the PT ring and GSH to the right. On the same tissue, protein markers specified the major cell types, immune cells, and cell states (Figure 4Aiii). With the image alignment and cell segmentation (Figure 4Aiv), the integrated omics in single cells were used for further discriminant analyses.

HCA elucidated the variation of monitored metabolites/lipids in different cell types and structural regions, namely CD45, LYVE-1, CD68, smooth muscle  $\alpha$ -Actin (SMA), and collagen I (Figure 4B). These markers were validated by IHC and detailed in STAR Methods<sup>39</sup> and Figure S3. Leukocytes (CD45 positive) were located mainly around the PT, sharing similar metabolism of high glucose consumption. Sinusoidal cells (LYVE-1 positive) comprise the higher ganglioside GM3 and PE species, which were highly relevant to cell adherence and mechanical resistance to highly packed cellular region.<sup>40,41</sup> Without distinct lipidomic and metabolic features, macrophage/Kupffer cells (CD68 positive) seemed to have slightly higher CLs. As a major tissue structure marker, SMA was co-localized with the PS 36:1-abundant region. The correlation of selected metabolites (heptanoic acid and heme B), lipids (PS 36:1), and proteins (CD4, CD45, CD68, and SMA) in 10 serial sections were presented in the fused 3D reconstruction of liver PT (Video S2).

t-SNE clustering was further applied to classify cells using protein and metabolites/lipids (Figures 4Ci and 4Cii, respectively). Clusters in gray and brown (Figure 4Cii) were consistent with collagen I- and SMA-positive areas (red, brown, and green clusters in Figure 4Ci). PP hepatocytes expressing Arg-1 and Alb (pink in Figure 4Ci) were sub-classified into clusters in orange, blue, magenta, and purple (Figure 4Cii). The result recapitulated that metabolites and lipids are efficient to characterize cell types and cell states.

### RNAscope, MALDI Orbitrap, and LC-MS/MS validate the core MSI workflow

To validate antibody markers used in the study, namely CD68, Glul, Alb, and LYVE1, single-molecule mRNA fluorescent *in situ* hybridization was performed on human liver tissue section. Color overlay images from RNAscope show the distribution of the RNA copies (Figures 2A and 2E), consistent with images of proteins in

Figure S3. For example, protein GS and its corresponding mRNA transcript, *Glul*, were localized around the CV but not the PV. In addition, fluorescent slide scanning allowed identification of the PV and CV, compared with H&E staining in mouse liver tissue (Figures 2 and S1B).

The identity of the zone-specific lipids was assessed using accurate mass match of the MSI-derived ions of interest against the library databases,<sup>42</sup> followed by UPLC-MS<sup>E</sup> fragment analysis from lipidomics analysis from liver tissue lipid extracts (Table 1). The analysis of DESI and lipidomics analysis with lock mass correction helps to align the precursor mass with high accuracy. The UPLC-MS<sup>E</sup> data were searched for the most commonly formed adducts, [M+ H<sup>+</sup>, Na<sup>+</sup>, K<sup>+</sup>]<sup>+</sup> in positive ion mode for DESI and [M-H]<sup>-</sup> for negative ion mode for both DESI and SIMS. The metabolites were annotated by accurate mass search against the library database<sup>43,44</sup> and ion mobility drift time of the standard when available. Most of the precursor ion matches between the DESI and LC-MS/MS were phospholipids and glycerolipids in positive ion mode, and those for SIMS were phospholipids in negative ion mode. Similarly, confirmation of lipid species based on MALDI is shown in Tables S1D and S1E. DESI and SIMS identified a complementary list of species around CV and PV (Tables 1), resulting from the difference in preferential ionization for different lipid species. High-resolution SIMS uncovered several metabolites and lipids that have a thin circular structure around both central and PVs, such as GSH, AMP, PE (40:6), PA (36:1), PS (38:3), and PI (38:4); some species were more concentrated inside veins, such as LPAs (Figures S2 and S4). DESI confirmed distinct distributions of free FAs, conjugated bile acids, and glycerolipids (Figures 2 and S1). Some species were validated by *in situ* tandem MS using MALDI (Tables S1D and S1E). However, metabolites and FAs were not validated by MALDI due to the mass interferences for species below *m/z* 350 from the matrix. These results demonstrate the complementary utility of a variety of MSI methods for more comprehensive imaging and annotation of biosamples.

## DISCUSSION

This study demonstrates major technological improvements that enable a multimodal workflow for multiplexed imaging of metabolites, lipids, and proteins for integrated spatial omics of anatomical structures at single-cell resolution. This multi-scale biomolecule detection works efficiently to distinguish anatomical features (e.g., CV, PV, and PT) and metabolic zones in liver tissue. Moreover, significant variations of species are observed in different types of liver cells, demonstrating that different metabolic states are needed for a spatial division of labor to efficiently manage a multitude of metabolic functions. Finally, we observed sex-specific differences in the distributions of many lipid species, suggesting that male and female mouse livers may be

(Aiii) Proteins image by lanthanides-conjugated antibodies from the same region after (H<sub>2</sub>O)<sub>n(n=30k)</sub>-GCIB-SIMS imaging, using C<sub>60</sub>-SIMS at spatial resolution of 1  $\mu$ m. Green, Alb; cyan, CD 68; lime green, CD45; red, LYVE-1; SMA, white; magenta, collagen I; blue, nuclei. (Aiii) The image alignment and registration of SIMS images (i.e., Aii and Aiii).

(Aiv) Registration of (H<sub>2</sub>O)<sub>n(n=30k)</sub>-GCIB-SIMS and C<sub>60</sub>-SIMS images for alignment; single-cell segmentation using DeepCell.

(B) HCA map shows the variation of different metabolites/lipids in different types of cells.

(C) (Ci) t-SNE clustering to classify the cell types as in cluster 1–8 by protein markers.

(Cii) t-SNE clustering to classify the cell types as in cluster 1–8 by lipids and metabolites only. Scale bars, 100  $\mu$ m.

**Table 1. Validation of lipid ion species from SIMS and DESI-MSI with MALDI-MSI and LC-MS/MS**

Pericentral vein region					Periportal vein region				
(H <sub>2</sub> O) <sub>n</sub> -GCIB-SIMS negative ion mode	MALDI orbitrap validation	LC-MS precursor mass	LC-MS/MS validation	(H <sub>2</sub> O) <sub>n</sub> -GCIB-SIMS negative ion mode	MALDI orbitrap validation	LC-MS precursor mass	LC-MS/MS validation		
303.23	FA C20:4	NA	NA	NA	255.23	FA C16:0	NA	NA	NA
311.23	FA C20:0	NA	NA	NA	279.23	FA C18:2	NA	NA	NA
742.53	PE 36:2	PE (18:0/18:2)	NA	NA	283.26	FA C18:0	NA	NA	NA
766.54	PE 38:4	PE (18:0/20:4)	NA	NA	514.28	Taurocholic acid	NA	NA	NA
911.56	PI 40:5	PI (18:0/22:5)	NA	NA	747.50	PA 40:6	PA (18:0/22:6)	747.48	PA 40:6
913.58	PI 40:4	PI 40:4	NA	NA	834.53	PS 40:6	PS (18:0/22:6)	834.53	PS 40:6
857.51	PI 36:4	PI (16:0/20:4)	NA	NA	835.53	PI 34:1	PI (12:0/22:1 (11Z))	835.53	PI 34:1
723.50	PA 38:4	PA (18:0/20:4)	723.48	PA 18:2/20:2	1454.03	CL 72:5	NA	NA	NA
810.53	PS 38:4	PS (18:0/20:4)	810.54	PS 38:4	1455.95	CL 72:4	NA	NA	NA
812.54	PS 38:3	NA	812.55	PS 38:3	1480.94	CL 74:6	NA	NA	NA
885.55	PI 38:4	PI (18:0/20:4)	885.55	PI 38:4	1482.08	CL 74:5	NA	NA	NA
-	-	-	-	-	1483.94	CL 74:4	NA	NA	NA
-	-	-	-	-	1484.98	CL 74:4	NA	-	-
DESI negative ion mode	MALDI orbitrap validation	LC-MS precursor mass	LC-MS/MS validation	DESI negative ion mode	MALDI orbitrap validation	LC-MS precursor mass	LC-MS/MS validation		
281.24	FA 18:1	NA	NA	NA	124.01	Taurine	NA	NA	NA
295.23	FA 18:2;O	NA	NA	NA	306.08	GSH	NA	NA	NA
293.21	FA 18:3;O	NA	NA	NA	762.51	PE 38:6	NA	762.50	PE 38:6
309.28	FA 20:1	NA	NA	NA	346.05	AMP/dGMP	NA	NA	NA
311.3	FA 20:0	NA	NA	NA	175.03	Ascorbic acid	NA	NA	NA
307.26	FA 20:2	NA	NA	NA	514.28	ST 24:1;O5;T	NA	NA	NA
-	-	-	-	-	512.27	Sulfoglycolithocholate	NA	NA	NA
-	-	-	-	-	498.29	ST 24:1;O4;T	NA	NA	NA
-	-	-	-	-	790.53	PE 40:6	PE (18:0/22:6)	790.53	PE 40:6
DESI positive ion mode	MALDI orbitrap validation	LC-MS precursor mass	LC-MS/MS validation	DESI positive ion mode	MALDI orbitrap validation	LC-MS precursor mass	LC-MS/MS validation		
647.46	DG 37:7	NA	647.45	DG 37:7	818.50	PC 36:5	PC 36:5	NA	NA
840.55	PC 39:7	NA	840.55	PC 39:7	756.54	PC 32:0	PC 34:3	756.54	PC 32:0
848.54	PC 38:4	PC 38:4	848.55	PC 38:4	560.31	LPC 18:1	NA	NA	NA
633.48	DG 34:1	NA	633.48	DG 34:1	562.32	LPC 18:0	PC 18:0	NA	NA
631.46	DG 34:2	NA	631.46	DG 34:2	518.32	LPC 16:0	PC 16:0	NA	LPC 16:0
659.49	DG 36:2	NA	659.49	DG 36:2	760.58	PC 34:1/PE 37:1	PC 34:1	NA	NA
657.48	DG 36:3	NA	657.48	DG 36:3	806.56	PC 38:6/PE 39:3	PC 36:3	NA	NA
655.46	DG 36:4	NA	655.46	DG 36:4	542.32	LPC 18:2	NA	NA	LPC 18:2
856.56	PC P-40:6	NA	856.55	PC P-40:6	786.59	PC 36:2	PE (36:2)	786.59	PC 36:2

functionally quite distinct, with implications for understanding sex-specific differences in disease risk and normal physiology. Further studies with a large sample size with different age groups could infer robust sex and liver zonation-specific lipid biomarkers.

Spatial metabolomics directly mirrors the cell metabolic phenotype and upstream genetic activities in health and disease. There is a growing interest in dissecting cellular and metabolic heterogeneity directly on tissue at single-cell resolution. This requires characterizing cell types and cell neighborhoods, as well as an atlas of biomolecule abundances within different cell types,

taking into account neighborhoods within the tissue architecture. However, there are few analytical tools to image multiple types of molecules in single cells directly on tissue without dissociation. Consecutive dual-SIMS imaging on the same frozen-hydrated tissue offers single-cell resolution and high chemical sensitivity to integrate spatial multi-omics (untargeted metabolomics and lipidomics and targeted proteomics) in the same individual cells on a single tissue at near-native state. With well-preserved gradients of small molecules, which would be otherwise diffused by chemical fixation and drying, the metabolic state of different types of cells can be revealed in liver tissue. In addition, cell

population separation on tissue directly by metabolic states has not been reported, but some success has been shown in classification of co-cultured cells by metabolic states using MALDI imaging and the computational approach SpaceM.<sup>45</sup> MALDI technology has also been further developed for high-resolution and high chemical sensitivity imaging at  $\leq 5 \mu\text{m}$  resolution.<sup>46</sup> The laser post-ionization enhances analytical sensitivity by up to several orders of magnitude, such as transmission-mode MALDI-2 MSI.<sup>47</sup> However, matrix application and incompatibility of cryogenic analysis may hinder its applications to single-cell metabolomics. It is also time-consuming to acquire high-resolution images in large samples (e.g., 3 days for one million pixels). Moreover, transmission-mode geometry technology is mostly in development mode with in-house setups. We adapted DESI in our workflow, owing to the simple sample preparation without matrix application, which minimizes the interference with small metabolic species.

With cryogenic dual-SIMS imaging at high resolution and data processing, we show that integrated metabolomic and lipidomic profiling in individual cells can be used for cell classifications without protein markers and tissue dissociation. As the role of individual lipid species are understudied, this platform could be extended to overlay spatial transcriptomics and proteomics, characterizing the distribution of enzymes involved in lipid metabolism to fully elucidate the spatial interaction and its functional significance. This will provide a rare opportunity to investigate previously unknown cellular subtypes and their unique protein-lipid-metabolite interactions.

Our multimodal pipeline with high-resolution multimodal MSI and computational processing has added layers of spatial omics about metabolic and lipidomic features in different types of cell populations, distinguishing subpopulations and distinct metabolic functions within individual cells on liver tissue. The workflow can be readily applied to liver disease samples for the discovery of metabolic dysregulation in different cell types, heterogeneous shift in the disease microenvironment, and cell-cell interactions, ultimately leading to therapeutic opportunities.

### Limitations of the study

The purpose of the study was to develop a multimodal imaging workflow to integrate multi-omics in the same sample to understand functional unit/cell-type-specific metabolic variation. The DESI and SIMS imaging on both mouse and human tissue were performed to validate the technique and data processing algorithm. However, there are some limitations to be overcome for future applications. First, we need to fit sufficient biological replicates in a reasonable time frame to draw any statistical significance. Our workflow takes advantage of faster DESI imaging to annotate the smaller areas of interest, which are for further high-resolution imaging using dual-SIMS. Therefore, biological replicates are feasible at varying levels of resolution, either tissue or cellular level. Second, *in situ* species confirmation is lacking. While the annotations of the lipid species were done by comparing the *m/z* values to accurate masses in the lipid and metabolite databases, and further validated by UPLC-HDMSE with molecular and fragmentation conformation, not all species that were observed in MSI could be found in the lipidomics library, and hence some of the annotations could be isomeric species, as noted in the supplemental tables. Last,

there are limited training datasets for cell segmentation to match all the cell types. Additional cell membrane markers could be used in the future to enhance the segmentation of cell types with varied morphologies.

### STAR★METHODS

Detailed methods are provided in the online version of this paper and include the following:

- KEY RESOURCES TABLE
- RESOURCE AVAILABILITY
  - Lead contact
  - Materials availability
  - Data and code availability
- EXPERIMENTAL MODEL AND STUDY PARTICIPANT DETAILS
- METHOD DETAILS
  - Tissue preparation
  - Histology
  - DESI MSI data acquisition and analysis
  - Untargeted Lipidomics sample preparation
  - Chromatographic separation and mass spectrometry analysis
  - Lipid and metabolite identification
  - Successive SIMS imaging and data processing; Cryogenic (H<sub>2</sub>O)<sub>n</sub>-GCIB-SIMS
  - Multiplex immunostaining
  - C<sub>60</sub>-SIMS
  - SIMS data processing
  - MALDI-MSI
  - RNAScope
- QUANTIFICATION AND STATISTICAL ANALYSIS

### SUPPLEMENTAL INFORMATION

Supplemental information can be found online at <https://doi.org/10.1016/j.devcel.2024.01.025>.

### ACKNOWLEDGMENTS

This research was supported by the National Institutes of Health (NIH) the Human BioMolecular Atlas Program (HuBMAP) (1UG3CA256962 and 4UH3CA256962). We thank our colleague, Dr. Andrea J. Radtke from the NIH, who provided insight and expertise in liver antibody panel. We would also like to show our gratitude to Dr. Dan Graham from the University of Washington and Dr. Nathan H. Patterson from Vanderbilt University for sharing their expertise in MSI data processing. We also thank Jacob Daniels from Columbia University for harvesting mouse liver used for the study.

### AUTHOR CONTRIBUTIONS

H.T., P.R., and B.R.S. conceived and designed the multimodal imaging workflow for liver tissue. H.T. conceived the dual-SIMS imaging workflow, established the lanthanide-conjugated antibody panel and immunostaining protocol, and performed tissue immunostaining, SIMS data acquisition, and general/discriminant processing. P.R. optimized sample processing for multimodal imaging, performed sample preparation, DESI imaging and data analysis, lipidomic experiments and data analysis, and multimodal data comparison. J.T. developed the software platform and algorithm for data processing, image registration, and segmentation under the supervision of H.T. A.M.D. performed RNAScope imaging and analysis. T.V.N. performed cryosectioning and assessed IHC data with P.R. T.A. performed MALDI imaging. F.Z.

contributed to lipidomic experiments. H.R. performed tissue identification, pathological analysis, and annotation of tissue structure. N.W. provided the SIMS instrumentation. H.T., P.R., and B.R.S. drafted and edited the paper. H.T. and B.R.S. supervised the project.

#### DECLARATION OF INTERESTS

B.R.S. is an inventor on patents and patent applications involving small-molecule drug discovery, ferroptosis, and immunostaining; holds equity in Sonata Therapeutics; co-founded and serves as a consultant to Exarta Therapeutics and ProJenX; and serves as a consultant to Weatherwax Biotechnologies Corporation and Akin Gump Strauss Hauer & Feld.

Received: September 16, 2022

Revised: May 11, 2023

Accepted: January 26, 2024

Published: February 14, 2024

#### REFERENCES

- HuBMAP Consortium (2019). The human body at cellular resolution: the NIH Human Biomolecular Atlas Program. *Nature* 574, 187–192.
- Rozenblatt-Rosen, O., Regev, A., Oberdoerffer, P., Nawy, T., Hupalowska, A., Rood, J.E., Ashenberg, O., Cerami, E., Coffey, R.J., Demir, E., et al. (2020). The Human Tumor Atlas Network: Charting Tumor Transitions across Space and Time at Single-Cell Resolution. *Cell* 181, 236–249.
- El-Achkar, T.M., Eadon, M.T., Menon, R., Lake, B.B., Sigdel, T.K., Alexandrov, T., Parikh, S., Zhang, G., Dobi, D., Dunn, K.W., et al. (2021). A multimodal and integrated approach to interrogate human kidney biopsies with rigor and reproducibility: guidelines from the Kidney Precision Medicine Project. *Physiol. Genomics* 53, 1–11.
- Börner, K., Teichmann, S.A., Quardokus, E.M., Gee, J.C., Browne, K., Osumi-Sutherland, D., Herr, B.W., 2nd, Bueckle, A., Paul, H., Haniffa, M., et al. (2021). Anatomical structures, cell types and biomarkers of the Human Reference Atlas. *Nat. Cell Biol.* 23, 1117–1128.
- Hickey, J.W., Neumann, E.K., Radtke, A.J., Camarillo, J.M., Beuschel, R.T., Albanese, A., McDonough, E., Hatler, J., Wiblin, A.E., Fisher, J., et al. (2022). Spatial mapping of protein composition and tissue organization: a primer for multiplexed antibody-based imaging. *Nat. Methods* 19, 284–295.
- Radtke, A.J., Kandov, E., Lowekamp, B., Speranza, E., Chu, C.J., Gola, A., Thakur, N., Shih, R., Yao, L., Yaniv, Z.R., et al. (2020). IBEX: A versatile multiplex optical imaging approach for deep phenotyping and spatial analysis of cells in complex tissues. *Proc. Natl. Acad. Sci. USA* 117, 33455–33465.
- Eberlin, L.S. (2014). DESI-MS imaging of lipids and metabolites from biological samples. *Methods Mol. Biol.* 1198, 299–311.
- Takáts, Z., Wiseman, J.M., and Cooks, R.G. (2005). Ambient mass spectrometry using desorption electrospray ionization (DESI): instrumentation, mechanisms and applications in forensics, chemistry, and biology. *J. Mass Spectrom.* 40, 1261–1275.
- Caprioli, R.M., Farmer, T.B., and Gile, J. (1997). Molecular imaging of biological samples: localization of peptides and proteins using MALDI-TOF MS. *Anal. Chem.* 69, 4751–4760.
- Djambazova, K.V., Klein, D.R., Migas, L.G., Neumann, E.K., Rivera, E.S., Van de Plas, R., Caprioli, R.M., and Spraggins, J.M. (2020). Resolving the Complexity of Spatial Lipidomics Using MALDI TIMS Imaging Mass Spectrometry. *Anal. Chem.* 92, 13290–13297.
- Tian, H., Sheraz Née Rabbani, S., Vickerman, J.C., and Winograd, N. (2021). Multiomics Imaging Using High-Energy Water Gas Cluster Ion Beam Secondary Ion Mass Spectrometry [(H<sub>2</sub>O)<sub>n</sub>-GCIB-SIMS] of Frozen-Hydrated Cells and Tissue. *Anal. Chem.* 93, 7808–7814.
- Tian, H., Sparvero, L.J., Anthonymuthu, T.S., Sun, W.Y., Amoscato, A.A., He, R.R., Bayir, H., Kagan, V.E., and Winograd, N. (2021). Successive High-Resolution (H<sub>2</sub>O)<sub>n</sub>-GCIB and C60-SIMS Imaging Integrates Multi-Omics in Different Cell Types in Breast Cancer Tissue. *Anal. Chem.* 93, 8143–8151.
- Tian, H., Sparvero, L.J., Blenkinsopp, P., Amoscato, A.A., Watkins, S.C., Bayir, H., Kagan, V.E., and Winograd, N. (2019). Secondary-Ion Mass Spectrometry Images Cardiolipins and Phosphatidylethanolamines at the Subcellular Level. *Angew. Chem. Int. Ed. Engl.* 58, 3156–3161.
- Trefts, E., Gannon, M., and Wasserman, D.H. (2017). The liver. *Curr. Biol.* 27, R1147–R1151.
- Kietzmann, T. (2017). Metabolic zonation of the liver: The oxygen gradient revisited. *Redox Biol.* 11, 622–630.
- Gebhardt, R., and Matz-Soja, M. (2014). Liver zonation: Novel aspects of its regulation and its impact on homeostasis. *World J. Gastroenterol.* 20, 8491–8504.
- Lamers, W.H., Hilberts, A., Furt, E., Smith, J., Jonges, G.N., van Noorden, C.J., Janzen, J.W., Charles, R., and Moorman, A.F. (1989). Hepatic enzymic zonation: a reevaluation of the concept of the liver acinus. *Hepatology* 10, 72–76.
- Aizarani, N., Saviano, A., Sagar, M., Maily, L., Durand, S., Herman, J.S., Pessaux, P., Baumert, T.F., and Grun, D. (2019). A human liver cell atlas reveals heterogeneity and epithelial progenitors. *Nature* 572, 199–204.
- Halpern, K.B., Shenav, R., Matcovitch-Natan, O., Toth, B., Lemze, D., Golan, M., Massasa, E.E., Baydatch, S., Landen, S., Moor, A.E., et al. (2017). Single-cell spatial reconstruction reveals global division of labour in the mammalian liver. *Nature* 542, 352–356.
- Kartsoli, S., Kostara, C.E., Tsimihodimos, V., Bairaktari, E.T., and Christodoulou, D.K. (2020). Lipidomics in non-alcoholic fatty liver disease. *World J. Hepatol.* 12, 436–450.
- Stopka, S.A., van der Reest, J., Abdelmoula, W.M., Ruiz, D.F., Joshi, S., Ringel, A.E., Haigis, M.C., and Agar, N.Y.R. (2022). Spatially resolved characterization of tissue metabolic compartments in fasted and high-fat diet livers. *PLoS One* 17, e0261803.
- Wang, F., Flanagan, J., Su, N., Wang, L.C., Bui, S., Nielson, A., Wu, X., Vo, H.T., Ma, X.J., and Luo, Y. (2012). RNAscope: a novel in situ RNA analysis platform for formalin-fixed, paraffin-embedded tissues. *J. Mol. Diagn.* 14, 22–29.
- Sirma, H., Williams, G.M., and Gebhardt, R. (1996). Strain- and sex-specific variations in hepatic glutamine synthetase activity and distribution in rats and mice. *Liver* 16, 166–173.
- Alexandrov, T., Becker, M., Deininger, S.O., Ernst, G., Wehder, L., Grasmair, M., von Eggeling, F., Thiele, H., and Maass, P. (2010). Spatial segmentation of imaging mass spectrometry data with edge-preserving image denoising and clustering. *J. Proteome Res.* 9, 6535–6546.
- Mandrekar, J.N. (2010). Receiver operating characteristic curve in diagnostic test assessment. *J. Thorac. Oncol.* 5, 1315–1316.
- Bradley, A.P. (1997). The use of the area under the roc curve in the evaluation of machine learning algorithms. *Pattern Recognit.* 30, 1145–1159.
- Ikeda, S., Tachikawa, M., Akanuma, S., Fujinawa, J., and Hosoya, K. (2012). Involvement of gamma-aminobutyric acid transporter 2 in the hepatic uptake of taurine in rats. *Am. J. Physiol. Gastrointest. Liver Physiol.* 303, G291–G297.
- Soares, A.F., Paz-Montoya, J., Lei, H., Moniatte, M., and Gruetter, R. (2017). Sexual dimorphism in hepatic lipids is associated with the evolution of metabolic status in mice. *NMR Biomed.* 30.
- Mittendorfer, B. (2005). Sexual dimorphism in human lipid metabolism. *J. Nutr.* 135, 681–686.
- Guzmán, M., and Castro, J. (1989). Zonation of fatty acid metabolism in rat liver. *Biochem. J.* 264, 107–113.
- Quistorff, B., Katz, N., and Witters, L.A. (1992). Hepatocyte heterogeneity in the metabolism of fatty acids: discrepancies on zonation of acetyl-CoA carboxylase. *Enzyme* 46, 59–71.
- Amigo, L., Mendoza, H., Zanlungo, S., Miquel, J.F., Rigotti, A., González, S., and Nervi, F. (1999). Enrichment of canalicular membrane with cholesterol and sphingomyelin prevents bile salt-induced hepatic damage. *J. Lipid Res.* 40, 533–542.

33. Simons, K., and Ehehalt, R. (2002). Cholesterol, lipid rafts, and disease. *J. Clin. Invest.* *110*, 597–603.
34. Longo, N., Frigeni, M., and Pasquali, M. (2016). Carnitine transport and fatty acid oxidation. *Biochim. Biophys. Acta* *1863*, 2422–2435.
35. Geisler, C.E., and Renquist, B.J. (2017). Hepatic lipid accumulation: cause and consequence of dysregulated glucoregulatory hormones. *J. Endocrinol.* *234*, R1–R21.
36. Paradies, G., Paradies, V., De Benedictis, V., Ruggiero, F.M., and Petrosillo, G. (2014). Functional role of cardiolipin in mitochondrial bioenergetics. *Biochim. Biophys. Acta* *1837*, 408–417.
37. Keren, L., Bosse, M., Marquez, D., Angoshtari, R., Jain, S., Varma, S., Yang, S.R., Kurian, A., Van Valen, D., West, R., et al. (2018). A Structured Tumor-Immune Microenvironment in Triple Negative Breast Cancer Revealed by Multiplexed Ion Beam Imaging. *Cell* *174*, 1373–1387.e19.
38. Amos, S.T.A., Kalli, A.C., Shi, J., and Sansom, M.S.P. (2019). Membrane Recognition and Binding by the Phosphatidylinositol Phosphate Kinase PIP5K1A: A Multiscale Simulation Study. *Structure* *27*, 1336–1346.e2.
39. Quardokus, E.M., Saunders, D.C., McDonough, E., Hickey, J.W., Werlein, C., Surette, C., Rajbhandari, P., Casals, A.M., Tian, H., Lowery, L., et al. (2023). Organ Mapping Antibody Panels: a community resource for standardized multiplexed tissue imaging. *Nat. Methods* *20*, 1174–1178.
40. Labrada, M., Dorvignit, D., Hevia, G., Rodríguez-Zhurbenko, N., Hernández, A.M., Vázquez, A.M., and Fernández, L.E. (2018). GM3(Neu5Gc) ganglioside: an evolution fixed neoantigen for cancer immunotherapy. *Semin. Oncol.* *45*, 41–51.
41. Calzada, E., Onguka, O., and Claypool, S.M. (2016). Phosphatidylethanolamine Metabolism in Health and Disease. *Int. Rev. Cell Mol. Biol.* *321*, 29–88.
42. Fahy, E., Subramaniam, S., Murphy, R.C., Nishijima, M., Raetz, C.R., Shimizu, T., Spener, F., van Meer, G., Wakelam, M.J., and Dennis, E.A. (2009). Update of the LIPID MAPS comprehensive classification system for lipids. *J. Lipid Res.* *50* (suppl), S9–S14.
43. Smith, C.A., O'Maille, G., Want, E.J., Qin, C., Trauger, S.A., Brandon, T.R., Custodio, D.E., Abagyan, R., and Siuzdak, G. (2005). METLIN: a metabolite mass spectral database. *Ther. Drug Monit.* *27*, 747–751.
44. Wishart, D.S., Guo, A., Oler, E., Wang, F., Anjum, A., Peters, H., Dizon, R., Sayeeda, Z., Tian, S., Lee, B.L., et al. (2022). HMDB 5.0: the Human Metabolome Database for 2022. *Nucleic Acids Res.* *50*, D622–D631.
45. Rappez, L., Stadler, M., Triana, S., Gathungu, R.M., Ovchinnikova, K., Phapale, P., Heikenwalder, M., and Alexandrov, T. (2021). SpaceM reveals metabolic states of single cells. *Nat. Methods* *18*, 799–805.
46. Zavalin, A., Yang, J., Hayden, K., Vestal, M., and Caprioli, R.M. (2015). Tissue protein imaging at 1  $\mu$ m laser spot diameter for high spatial resolution and high imaging speed using transmission geometry MALDI TOF MS. *Anal. Bioanal. Chem.* *407*, 2337–2342.
47. Niehaus, M., Soltwisch, J., Belov, M.E., and Dreisewerd, K. (2019). Transmission-mode MALDI-2 mass spectrometry imaging of cells and tissues at subcellular resolution. *Nat. Methods* *16*, 925–931.
48. Bannon, D., Moen, E., Schwartz, M., Borba, E., Kudo, T., Greenwald, N., Vijayakumar, V., Chang, B., Pao, E., Osterman, E., et al. (2021). DeepCell Kiosk: scaling deep learning-enabled cellular image analysis with Kubernetes. *Nat. Methods* *18*, 43–45.
49. Kessner, D., Chambers, M., Burke, R., Agus, D., and Mallick, P. (2008). ProteoWizard: open source software for rapid proteomics tools development. *Bioinformatics* *24*, 2534–2536.
50. Race, A.M., Styles, I.B., and Bunch, J. (2012). Inclusive sharing of mass spectrometry imaging data requires a converter for all. *J. Proteomics* *75*, 5111–5112.
51. Sud, M., Fahy, E., Cotter, D., Brown, A., Dennis, E.A., Glass, C.K., Merrill, A.H., Jr., Murphy, R.C., Raetz, C.R., Russell, D.W., et al. (2007). LMSD: LIPID MAPS structure database. *Nucleic Acids Res.* *35*, D527–D532.
52. Beare, R., Lowekamp, B., and Yaniv, Z. (2018). Image Segmentation, Registration and Characterization in R with SimpleITK. *J. Stat. Softw.* *86*, 8.

STAR★METHODS

KEY RESOURCES TABLE

REAGENT or RESOURCE	SOURCE	IDENTIFIER
<b>Antibodies</b>		
89Y CD45(Mu)	Fluidigm	Cat# 3089005B; RRID: AB_2651152
142Nd Heppar-1/CPS1(Mu)	Novus	Cat# NBP3-08970; RRID: AB_2909615
143Nd GFAP(Mu)	Abcam	Cat# ab218309; RRID: AB_2909614
147Sm GS (Mu)	Abcam	Cat# ab240193; RRID: AB_2909636
152Sm F4/80(Mu)	Abcam	Cat# ab6640; RRID: AB_1140040
155Gd CD11b(Mu)	lonpath	Cat# 715503-100; RRID: AB_3086752
156Gd CD68(Mu)	Abcam	Cat# ab237968; RRID: AB_3086750
174Yb LYVE1(Mu)	Novus	Cat# NB600-1008; RRID: AB_10000497
176Yb EGFR(Mu)	Abcam	Cat# ab272293; RRID: AB_2909619
176Yb Na/K ATPase(Mu)	Abcam	Cat# ab167390; RRID: AB_2890241
191 Ir Nuclear DNA(Mu)	Fluidigm	Cat# 201192B; RRID: AB_3086753
89Y CD45 (Hu)	Cell Signaling	Cat# 13917S; RRID: AB_3086754
141Pr SMA(Hu)	Fluidigm	Cat# 3141017D; RRID: AB_2890139
145Nd Heppar-1/CPS1(Hu)	Novus	Cat# NBP3-08970; RRID: AB_2909615
147Sm GS (Hu)	Abcam	Cat# ab240193; RRID: AB_2909636
148Nd CD31(Hu)	Abcam	Cat# ab264090; RRID: AB_2909616
151Eu CD68(Hu)	Cell Signaling	Cat# 76437S; RRID: AB_2909615
153Eu CD32(Hu)	Fluidigm	Cat# 3153018B; RRID: AB_2909617
158Gd Arginase1(Hu)	Cell Signaling	Cat# 93668S; RRID: AB_3086760
161Dy Albumin(Hu)	Abcam	Cat# Ab271979; RRID: AB_2909637
169Tm CD34(Hu)	Abcam	Cat# ab198395; RRID: AB_2889381
171Yb LYVE1(Hu)	Abcam	Cat# ab232935; RRID: AB_2889891
176Yb EGFR(Hu)	Abcam	Cat# ab272293; RRID: AB_2909619
176Yb Na/K ATPase (Hu)	Cell Signaling	Cat# 23565S; RRID: AB_3086761
191 Ir Nuclear DNA(Hu)	Fluidigm	Cat# 201192B; RRID: AB_3086753
196Pt Collagen I(Hu)	Abcam	Cat# ab215969; RRID: AB_2909621
Mm-Alb-C2 (RNA scope)	ACD Bio	437691-C2
Mm-GluI (RNA scope)	ACD Bio	426231
Mm-Ptprc-C3 (RNA scope)	ACD Bio	318651-C3
Hs-GLUL-No-XMm (RNA scope)	ACD Bio	511171
Hs-CD68-C4 (RNA scope)	ACD Bio	560591-C4
Hs-LYVE1 (RNA scope)	ACD Bio	426911
<b>Biological samples</b>		
Healthy mouse liver	Charles River	17 weeks old male (n=3) and female (n=3) C57/BL6 mice
Healthy human liver	Columbia University tissue bank	51-year-old female
<b>Deposited data</b>		
SIMS data	Scholarsphere	<a href="https://doi.org/10.26207/6a38-tr35">https://doi.org/10.26207/6a38-tr35</a>
DESI positive mode human liver data	HuBMAP data portal	<a href="https://doi.org/10.35079/HBM875.FTTV.999">https://doi.org/10.35079/HBM875.FTTV.999</a>

(Continued on next page)

**Continued**

REAGENT or RESOURCE	SOURCE	IDENTIFIER
DESI negative mode human liver data	HuBMAP data portal	<a href="https://doi.org/10.35079/HBM238.PWFH.224">https://doi.org/10.35079/HBM238.PWFH.224</a>
SIMS 3D liver construction	HuBMAP consortium	<a href="https://portal.hubmapconsortium.org/preview/multimodal-mass-spectrometry-imaging-data">https://portal.hubmapconsortium.org/preview/multimodal-mass-spectrometry-imaging-data</a>

**Software and algorithms**

Ionoptika Image Analyzer	Ionoptika Ltd.	<a href="https://ionoptika.com">https://ionoptika.com</a>
ImagingSIMS	Jay Tarolli	<a href="https://github.com/ImagingSIMS/ImagingSIMS">https://github.com/ImagingSIMS/ImagingSIMS</a>
DeepCell	Bannon et al. <sup>48</sup>	<a href="https://deepcell.com/">https://deepcell.com/</a>
SCiLS	Bruker Corp.	<a href="https://www.bruker.com/">https://www.bruker.com/</a>
Progenesis	Waters Corp.	<a href="https://www.waters.com/">https://www.waters.com/</a>
MS <sup>E</sup> Dataviewer	Waters Corp.	<a href="https://www.waters.com/">https://www.waters.com/</a>

**Other**

Multimodal imaging pipeline	N/A	<a href="https://dx.doi.org/10.17504/protocols.io.kxygx913zg8j/v1">https://dx.doi.org/10.17504/protocols.io.kxygx913zg8j/v1</a>
Cryosectioning fresh frozen tissues for multimodal imaging	N/A	<a href="https://dx.doi.org/10.17504/protocols.io.e6nvwjnjzlmk/v1">https://dx.doi.org/10.17504/protocols.io.e6nvwjnjzlmk/v1</a>
DESI imaging mass spectrometry on liver tissue	N/A	<a href="https://dx.doi.org/10.17504/protocols.io.ewov1nze7gr2/v1">https://dx.doi.org/10.17504/protocols.io.ewov1nze7gr2/v1</a>
Immunohistochemistry of liver tissue sections	N/A	<a href="https://dx.doi.org/10.17504/protocols.io.5qpvo1k9l4o/v1">https://dx.doi.org/10.17504/protocols.io.5qpvo1k9l4o/v1</a>
Cryogenic (H <sub>2</sub> O)n-GCIB-SIMS imaging	N/A	<a href="https://dx.doi.org/10.17504/protocols.io.81wgbyynovpk/v1">https://dx.doi.org/10.17504/protocols.io.81wgbyynovpk/v1</a>
Liver tissue staining with multiple lanthanides-tagged antibodies	N/A	<a href="https://dx.doi.org/10.17504/protocols.io.b5qmq5u6">https://dx.doi.org/10.17504/protocols.io.b5qmq5u6</a>
RNAscope spatial transcript imaging	N/A	<a href="https://dx.doi.org/10.17504/protocols.io.kqdg3p3e7l25/v1">https://dx.doi.org/10.17504/protocols.io.kqdg3p3e7l25/v1</a>

**RESOURCE AVAILABILITY**

**Lead contact**

Requests for further information and resources should be directed to the lead contact, Prof. Brent R. Stockwell ([bstockwell@columbia.edu](mailto:bstockwell@columbia.edu)).

**Materials availability**

This study did not generate new unique reagents.

**Data and code availability**

- Mass spectrometry imaging raw data are available in standardized imzML format. SIMS data is available at <https://doi.org/10.26207/6a38-tr35>. The imzml and selected ion images from DESI is available from <https://portal.hubmapconsortium.org>. The software license is provided for analyzing the data using Ionoptika Analyser for up to 7 days. Please contact Ionoptika if you wish to use the software beyond 7 days via our Support e-mail ([support@ionoptika.co.uk](mailto:support@ionoptika.co.uk)). Accession numbers are listed in the [key resources table](#).
- Any additional information required to reanalyze the data reported in this work paper is available upon request.

**EXPERIMENTAL MODEL AND STUDY PARTICIPANT DETAILS**

Normal human liver sample from a 51-year-old female was retrieved from the Columbia University tissue bank, under a protocol approved by the Institutional Review Board. Informed consent was obtained from the human sample for use of the tissue in research. Mouse liver tissues were derived from 17 weeks old male (n=3) and female (n=3) C57BL/6 mice, under an approved IACUC protocol. Mice were housed at a maximum of 5 mice per cage on irradiated bedding (Bed-O'Cobs® bedding, WF Fisher and Son, Somerville, NJ) in ventilated microisolator cages. Mice were provided with irradiated Enviro-Dri for nesting material. Mice had access to

autoclaved or RO water and irradiated pelleted diet ad libitum. Mice were pathogen-free and were maintained in accordance with the Guide for the Care and Use of Laboratory Animals in an AAALAC-accredited facility.

## METHOD DETAILS

### Tissue preparation

The excised liver tissues were flash frozen on dry ice filled with hexane and stored at  $-80^{\circ}\text{C}$  until use. Small blocks of both human and mouse tissue were cryosectioned at  $8\text{-}10\mu\text{m}$  thickness and thaw mounted on microscope glass slides for H&E, DESI and RNAScope analysis and gold-coated slides for SIMS analysis. For multimodal imaging, consecutive sections for DESI, H&E, SIMS, and RNAScope were placed on the respective slides and stored at  $-80^{\circ}\text{C}$  until analysis.

### Histology

Tissue sections were stained with hematoxylin and eosin (H&E) staining at Columbia University Molecular Pathology Shared Resource facility, scanned at 20X magnification and histological examination was performed by a pathologist to annotate the anatomical structures.

### DESI MSI data acquisition and analysis

All the experiments were performed on Synapt G2-Si QToF mass spectrometer (Waters, Milford, MA), coupled to a DESI ion source. Data was acquired in sensitivity mode in both positive and negative ion mode with mass range of  $m/z$  100-1000. The DESI parameters used were capillary voltage and sampling cone voltage of 0.65kV and 50V respectively, scan time of 0.145 sec/pixel, pixel size of  $40\mu\text{m}^2$ , DESI sprayer angle of  $75^{\circ}$ , nebulizing gas ( $\text{N}_2$ ) pressure of 0.3 PSLM. The solvent used was methanol: water 95:5 (v/v) with 0.01% formic acid and 20pg/ $\mu\text{l}$  leucine enkephalin, at a flow rate of 1.5  $\mu\text{l}/\text{min}$ . Tissue sections were dried in a desiccator for  $\sim 10$  min prior to analysis. Peak picking and lockmass correction using the protonated ion of leucine enkephalin ( $[\text{M}+\text{H}]^+$ ,  $m/z$  556.2771) or the deprotonated molecular ion ( $[\text{M}-\text{H}]^-$ ,  $m/z$  554.2615) was implemented in MassLynx software (Waters, version 4.1). The centroided data files were converted to mzml using msconvert from Proteowizard<sup>49</sup> followed by conversion to imzml format using imzMLConverter.<sup>50</sup> The imzml files were imported into the SCiLS lab software (Bruker, version 2021c) and subsequent data analysis was performed. Total ion count (TIC) normalization was performed and up to  $n$  peaks were selected of  $m/z$  intervals of  $\pm 0.03\text{Da}$  were selected. Spatial segmentation analysis was performed using bisecting k-means clustering on edge-preserving denoised data. Area under the receiver operator characteristic curve was also performed within the SCiLS platform.

### Untargeted Lipidomics sample preparation

20 mg of liver was homogenized using beadrupter and lipids were extracted using 1050ul of 1:2 ratio of ice-cold methanol containing 0.01% w/v butylated hydroxyl toluene and dichloromethane, vortex mixing and incubating the samples overnight at  $-20\text{C}$ . One volume of ice-cold water was added and mixed for phase separation followed by centrifugation. The lower organic phase containing lipids were collected in a new vial, dried under a gentle stream of nitrogen and stored at  $-80\text{C}$  until analysis. The samples were reconstituted in isopropanol: acetonitrile: water at the ratio of 11:9:2 v/v/v before analysis.

### Chromatographic separation and mass spectrometry analysis

Lipidomics experiments were performed on Synapt G2-Si mass spectrometer equipped with Acquity UPLC system (Waters, Milford, MA) in both positive and negative electrospray ion modes. The chromatographic separation was performed on Acquity UPLC BEH300 C18 column ( $1.7\mu\text{m}$  particle size,  $2.1\times 100\text{mm}$ ) (Waters, Milford, MA) over an 18 min gradient. The column temperature was set at  $55\text{C}$ . A binary mobile phase consisted of (A) 60:40 v/v acetonitrile: water and (B) 85:10:5 v/v/v isopropanol/acetonitrile/water, each containing 10mM ammonium acetate and 0.1% acetic acid. The gradient was initiated at 40% B, followed by linear gradient to 50% by 2min ramped up to 99%B by 18min, and the column was equilibrated for 2min to the initial condition. The flow rate was set at 400ul/min and injection volume was 2ul in positive mode and 5ul in negative mode. Data was acquired on high-definition data independent mode with ion mobility (HDMS<sup>E</sup>), over the mass range of  $m/z$  50 to 1200 Da and scan rate of 0.1sec per scan. The parameters used for mass spectrometry data acquisition is as follows: for positive and negative mode, capillary voltage and sampling cone voltage of 2.8kV and 35V; and 2.5kV and 32V were used respectively. The source and desolvation temperature were  $120^{\circ}\text{C}$  and  $500^{\circ}\text{C}$  respectively. Desolvation gas ( $\text{N}_2$ ) flow was set at 850 L/hr. MS data was calibrated using leucine encephalin infusion at a flow rate of 10ul/min. Default ion mobility settings were used. The low collision energy was set at 4 eV and high energy was 25-60 eV. Mass calibration was performed using sodium formate and collision cross section (CCS) calibration was performed using CCS Major mix (Waters).

### Lipid and metabolite identification

The assignment of lipids and metabolites specific of selected ions from DESI-MSI were based on its assignment based on accurate mass and isotopic pattern score using Progenesis software (Waters Inc., Milford, MA). The accurate mass search against the available databases including Lipidmaps,<sup>35</sup> HMDB<sup>44</sup> and Metlin<sup>43</sup> for  $[\text{M}+(\text{H}/\text{Na}/\text{K})]^+$  adducts were searched in positive ion mode and  $[\text{M}-\text{H}]^-$  adducts in negative ion mode. For UPLC-HDMS<sup>E</sup> lipidomics data, the assignment of the lipid features was based on

retention time information, accurate mass as well as fragmentation information. Fragmentation match was made in Progenesis software, where fragmentation score and match were assessed. It was also performed in MS<sup>E</sup> dataviewer (Waters, Milford, MA), where the fragments were confirmed against the Lipidmaps structure database (LMSD)<sup>51</sup> for the adducts mentioned above. Finally, the accurate mass of DESI-MSI based ion was matched against the UPLC-HDMS<sup>E</sup> data for assignment. Annotation of small metabolites and lipid species not detected by LC-MS/MS were based on accurate mass match of precursor ion.

### Successive SIMS imaging and data processing; Cryogenic (H<sub>2</sub>O)<sub>n</sub>-GCIB-SIMS

Both (H<sub>2</sub>O)<sub>n</sub>-GCIB and C<sub>60</sub>-SIMS were performed on a buncher-ToF instrument, J105 3D Chemical Imager (Ionoptika, Southampton, UK. Abbv. J105). The water cluster ion beam is pulsed through a pulser in the gun column, where the distance to the sample surface is 0.533 m. Beam tuning was assisted with an oscilloscope (Tektronix TDS 2024, USA) with detection by a secondary electron detector (SED). The singly-charged (H<sub>2</sub>O)<sub>n</sub> cluster size at beam energy of 70 kV with a time of flight (ToF) of 103 μs was calculated using the ToF equation as  $n = 30,900$ . The SED offset was 8 μs. Beam focus was measured by scanning a 1000 mesh grid (Agar Scientific, Essex, UK). The average beam spot sizes were calculated using 20/80 percent of maximum intensities and were  $1.60 \pm 0.01$  μm and  $1.16 \pm 0.45$  μm for 70 keV (H<sub>2</sub>O)<sub>30k</sub><sup>+</sup> and 40 kV C<sub>60</sub><sup>+</sup>, respectively. The beam dither was adapted to match the image pixel size. The mass resolution  $m/\Delta m$  was 6875 around  $m/z$  100, and 10,000~12,000 up to  $m/z$  2000. The live readout of mass resolution was from the software, Ionoptika SIMS Mainframe during the data acquisition.

The gold coated Si wafer with the frozen-hydrated mouse/human liver tissue section was plunged into liquid nitrogen and inserted to the pre-chilled cold sample stage in J105 instrument and kept at 100 K during GCIB-SIMS imaging. This cryogenic sample handling preserved the frozen-hydrated state thus maintaining the chemical gradients in the tissue section.

Guided by the anatomical features on the semi-serial H&E stained section, an area of interest was selected for SIMS imaging in negative ion mode using a 70 keV (H<sub>2</sub>O)<sub>30k</sub><sup>+</sup> beam. The acquisition was in negative ion mode with 256 × 256 pixels using a 2 × 2 tiled image mode for mouse liver tissue sections, or 768 × 768 pixels using a 3 × 3 tiled image mode for human liver tissue sections. Each tile covered 400 × 400 μm<sup>2</sup> (3.1 μm per pixel) for each section. The larger pixel size than the beam focus was used to image a broader area within practical time frame and to facilitate the charge neutralization by low energy (15 eV) electron beam. 1 pA of beam current and 296 shots per pixel, the ion doses were  $3.01 \times 10^{12}$  ions/cm<sup>2</sup> each tile.

### Multiplex immunostaining

The antibody panel, designed to identify the major cell types, immune cells, cell proliferation, structure and nuclei within the liver is described in [key resources table](#). Briefly, after the (H<sub>2</sub>O)<sub>n</sub>-GCIB-SIMS profiling was performed, the frozen tissue was placed at -20 °C and 4 °C consecutively for 1 h each for temperature equilibration, followed by fixation in 4 % formalin solution at 4 °C for 30 min. Non-specific protein binding was blocked with 3 % BSA (Bovine Serum Albumin) for 45 min at room temperature. Overnight staining was then performed with the antibody cocktail solution (750 ug/mL for each antibody) at 4 °C. The stained slide was washed with 0.2 % Triton X-100 in PBS (phosphate-buffered saline) 1X for 8 min before the final nuclear staining with Intercalator-Ir at 300 μL/section. After washing with double-distilled water for 10 min and air-drying for 30 min, the slide was again inserted into the SIMS instrument, this time for C60 imaging. For immunohistochemistry, briefly, tissue sections were fixed in cold acetone, washed, and incubated with 30% hydrogen peroxide. The sections were blocked with 10% goat serum and incubated with primary antibody for 90 mins followed by biotinylated secondary antibody at room temperature, with washing steps in between. This was followed by addition of avidin-biotin complex reagent and then DAB (3,3'-Diaminobenzidine) with washing between steps. The stained slide was washed with water and counterstained with hematoxylin, mounted with coverslip and scanned at 20x resolution.

### C<sub>60</sub>-SIMS

High resolution images using 40 keV C<sub>60</sub><sup>+</sup> were then acquired on the same area previously profiled by the (H<sub>2</sub>O)<sub>n</sub>-GCIB-SIMS. The acquisition was conducted in positive mode to localize various cell types. This was achieved by spatially detecting unique  $m/z$  ions of the isotopic metal tags associated with cell-specific antibodies. To resolve single cells, the C<sub>60</sub><sup>+</sup> beam was finely focused to 1.0 μm to image roughly the same area which has been analyzed by (H<sub>2</sub>O)<sub>n</sub>-GCIB. With the beam current of 5 pA and 1000 shots per pixel, the ion dose was  $8.57 \times 10^{13}$  ions/cm<sup>2</sup>. The dwell time was 100 ms/pixel. The lanthanide tags from eight antibodies and the nuclear marker were detected at an adequate signal intensity to allow co-registration with lipid and metabolite ions detected by (H<sub>2</sub>O)<sub>n</sub>-GCIB-SIMS.

### SIMS data processing

Single mass channels from tiled C<sub>60</sub> and (H<sub>2</sub>O)<sub>n</sub>-GCIB-SIMS images were extracted using Ionoptika Image Analyser (Version 2.0.2.11) and subsequently used for downstream processing, all performed with custom developed Python code. The ion assignment of metabolites and lipids were performed by  $m/z$  matching and further validation of certain species were done by LC-MS and MALDI orbitrap. Co-registration of C<sub>60</sub> and (H<sub>2</sub>O)<sub>n</sub>-GCIB-SIMS images was by first selecting mass channels that demonstrated a representative morphology of the tissue and normalizing each to an intensity range of [0, 1]. Normalized images were registered using SimpleITK<sup>52</sup> (v 2.0.2) to determine the best affine transform between the C<sub>60</sub> (fixed) and H<sub>2</sub>O (moving) images by minimizing the mean square difference using a gradient descent optimizer. All H<sub>2</sub>O channel data was then transformed to the C<sub>60</sub> image space. The general nuclear and membrane channels from the C<sub>60</sub> data set were then used to segment single cells using DeepCell<sup>48</sup> (v 0.9.0). Since the (H<sub>2</sub>O)<sub>n</sub>-GCIB-SIMS data has been registered to the C<sub>60</sub> image space, the segmentation instances can be used to extract

integrated counts of species in both SIMS data sets. Integrated protein expression from  $C_{60}$ -SIMS images was used to determine thresholds for cell classification (marker positive or negative). Hierarchical clustering analysis (HCA) was performed with *seaborn* (v 0.11.1) on the integrated lipid and metabolite mass channels from the  $(H_2O)_n$ -GCIB-SIMS data set, using the cell types determined from the  $C_{60}$  image data. The Algorithms of the data processing can be downloaded from the shared resources as in Software and algorithms of [key resources table](#).

To create a 3D visualization of the lipid, metabolite, and protein information, all SIMS images were registered into the same image space. First, each depth of the z-stack for the  $C_{60}$ -SIMS protein images was co-registered into the image space of the first layer. Then, the  $(H_2O)_n$ -GCIB-SIMS lipid and metabolite images were co-registered at each depth to the previously registered  $C_{60}$ -SIMS protein image from that depth. The resampled  $C_{60}$ -SIMS and  $(H_2O)_n$ -GCIB-SIMS image data for each depth was saved as a CSV file, imported into *ImagingSIMS* (version 3.8.1.1) and used to define a volume for each protein, lipid, and metabolite species of interest. These volumes were combined and rendered using volume raycasting of the scalar volume data.

### MALDI-MSI

Chemicals and solvents (analytical grade) were purchased from the following sources:  $\alpha$ -Cyano-4-hydroxycinnamic acid 98% (CHCA) (Sigma Aldrich), 1,5-Diaminonaphthalene 97% (DAN) (Sigma Aldrich), acetonitrile (ACN) (Honeywell), chloroform (Acros Organics), methanol (Carl Roth), and trifluoroacetic acid (TFA) (Sigma Aldrich). All chemicals used in this study were stored, handled, and disposed of according to good laboratory practices (GLP).

Mouse and human liver sections on ITO glass (Sigma, Milwaukee, WI, US) were stored at  $-80^\circ\text{C}$  until analysis. Prior to matrix application, the tissue sections were removed from the freezer, placed on a cold steel plate ( $-20^\circ\text{C}$ ) and freeze-dried in a desiccator for 30 minutes. The combination of steel plate and desiccator was efficient for removing the water from the tissue without compromising its structural integrity and limiting the migration of analytes. On the mouse liver section, DAN matrix (10 mg/ml, ACN:H<sub>2</sub>O 7:3) was applied. For the analysis of human liver, 2 sections were coated in matrix, one with DAN (same as mouse) for negative ion mode and one with CHCA matrix (5mg/ml, CHCl<sub>3</sub>:MeOH 1:1) for positive ion mode analysis. Application was performed with an HTX TM sprayer (HTX Technologies LLC, USA), temperature:  $30^\circ\text{C}$  (Dan)/  $40^\circ\text{C}$  (CHCA), passes: 8 (DAN)/16 (CHCA), flow rate: 0.12 ml/min, velocity: 1200 mm/min, drying time: 2 s, line spacing 2.5 mm.

AP-MALDI analysis was performed using an AP-MALDI UHR ion source (Masstech Inc., USA), which has been described in detail elsewhere,<sup>40,41</sup> coupled to an LTQ/Orbitrap Elite high-resolution mass spectrometer (Thermo-Fisher Scientific, USA) in positive and negative ion mode. For imaging, the AP-MALDI source was operated in "Constant Speed Raster" motion mode. To explore the detectable species and instrument settings for both ion modes, one whole mouse liver section was analyzed interlaced in positive and negative ion mode with a laser beam diameter of 20  $\mu\text{m}$  and a stepping size of 50  $\mu\text{m}$ , laser settings 2500 Hz, 5%. Spectrum acquisition parameters were 800 ms maximum injection time, mass range: 500 – 2000 Da and mass resolution: 120k at  $m/z$  400. Human liver was analyzed with higher spatial resolution (15  $\mu\text{m}$  laser spot and stepping size) and positive (CHCA matrix, laser settings 500 Hz, 10%) and negative (DAN matrix, laser settings 1500 Hz, 5%) ion mode analysis was performed on 2 separate, consecutive sections. Spectrum acquisition was adjusted to 500 ms maximum injection time, mass range: 350 – 1550 Da and mass resolution: 120k at  $m/z$  400. Species identification was performed with on-tissue tandem-MS with a 1.5 Da isolation window, and collision-induced dissociation/ higher-energy collision dissociation (CID/HCD) was performed with collision energies of 27-45%, adjusted for each species individually. Tandem-MS scans were summed up over 30-120 seconds. Data analysis and visualization was performed with Thermo Xcalibur 2.2 (Thermo-Fisher Scientific, USA), MultimagingTM (ImaBiotech, France), METASPACE,<sup>42</sup> and LipostarMSI (Molecular Horizons Srl, Italy).<sup>43</sup> Lipid identification was performed in LipostarMSI (database: LIPIDMAPS, mass accuracy: 2 ppm; mass and isotopic pattern score: 80%+).

### RNA Scope

We captured transcription distributions of select liver cell marker genes via *in situ* hybridization of specific targeting probes with the RNA Scope Multiplex Fluorescent v2 Assay Protocol<sup>27</sup> optimized for fresh-frozen samples. Our modifications to the commercial protocol included using half-concentration wash buffer (0.5X) for all wash steps downstream of probe incubation and excluding the recommended protease step entirely. In mouse tissue, we spatially detected the transcripts for, ALB (Albumin), GLUL (Glutamine synthetase), and PTPRC (Protein Tyrosine Phosphatase Receptor Type C), and in human tissue, we spatially detected transcripts for GLUL, CD68 (Macrophage Antigen CD68), and LYVE1 (Lymphatic Vessel Endothelial Hyaluronan Receptor 1).

Tissue sections were first post-fixed with 4% paraformaldehyde (PFA) in phosphate buffered saline (PBS) and dehydrated in Ethanol (EtOH) immediately after fixation, immersed for 5 minutes at a time in 50% EtOH, 70% EtOH, 100% EtOH, and 100% EtOH an additional time. Samples were then air-dried and treated with RNA Scope® Hydrogen Peroxide Reagent for ten minutes at  $23^\circ\text{C}$  to  $25^\circ\text{C}$  and washed twice with deionized water. Importantly, we excluded the commercial protease step because tissue integrity was lost, and we could achieve stronger signal without any protease treatment. These steps constitute the pretreatment steps.

These pre-treated sample slides were incubated with prewarmed target probes (20 nmol/L of each oligo probe) overnight. In mouse tissue, ALB was targeted with RNA Scope® Probe- Mm-Alb-C2 (ACD;Cat No. Cat No. 437691-C2), GLUL was targeted with RNA Scope Probe- Mm-Glul (ACD;Cat No. 426231), and PTPRC was targeted with RNA Scope® Probe- Mm-Ptprc-C3

(ACD;Cat No. 318651-C3). In human tissue, GLUL was targeted with RNAscope® Probe- Hs-GLUL-No-XMm (ACD;Cat No. Cat No. 511171), CD68 was targeted with RNAscope® Probe- Hs-CD68-C4 (ACD;Cat No. 560591-C4), and LYVE1 was targeted with RNAscope® Probe- Hs-LYVE1 (ACD;Cat No. 426911).

The tissue was incubated in the primary target probes overnight (18–21 hours) at 40°C inside the HybEZ hybridization oven (ACD). After overnight probe hybridization, samples were incubated in Amplifier 1 (preamplifier) (2 nmol/L) in hybridization buffer B (20% formamide, 5× SSC, 0.3% lithium dodecyl sulfate, 10% dextran sulfate, blocking reagents) for 30 minutes; Amplifier 2 (2 nmol/L) in hybridization buffer B at 40°C for 15 minutes; and Amplifier 3 (label probe) (2 nmol/L) in hybridization buffer C (5× SSC, 0.3% lithium dodecyl sulfate, blocking reagents) for 15 minutes. After each hybridization step, slides were washed with 0.5X wash buffer (0.05× SSC, 0.015% lithium dodecyl sulfate) two times at room temperature. Chromogenic detection was performed utilizing a horseradish peroxidase (HPR) construct specific to each gene-dedicated imaging channel and a fluorescent Opal reagent of choice. For the mouse sections, ALB was stained with Opal 520 Reagent (Perkin Elmer, FP1487001KT), GLUL was stained with Opal 570 Reagent (Perkin Elmer, FP1488001KT), and PTPRC was stained with Opal 690 Reagent (Perkin Elmer, FP1488001KT). For the human sections, GLUL and LYVE1 were both stained with Opal 520 Reagent (Perkin Elmer, FP1487001KT), thus needing to be imaged in separate tissue sections, and CD68 was stained with Opal 570 Reagent (Perkin Elmer, FP1488001KT). Each Opal reagent dye was diluted 1:1500 in RNAscope® Multiplex TSA Buffer. Nuclei were stained with DAPI (4',6-diamidino-2-phenylindole) and coverslips were mounted over slides in Fluoro-Gel (EMS; 17985-10) and imaged by spinning disc confocal microscopy and an Aperio Versa 8 fluorescent slide scanner.

### QUANTIFICATION AND STATISTICAL ANALYSIS

Mass spectrometry imaging data shows the relative signal intensity, counts/pixel showing relative distribution of ions within the image. The zonal difference in DESI based ion intensities between male and female mice liver were based on 3 independent samples from each group where standard deviation was used as a statistical measure. HCA method is the main algorithm used in this paper to compare the intensity differences of different metabolites/lipids species in functional units and different cell types from SIMS data.